



저작자표시-비영리-변경금지 2.0 대한민국

이용자는 아래의 조건을 따르는 경우에 한하여 자유롭게

- 이 저작물을 복제, 배포, 전송, 전시, 공연 및 방송할 수 있습니다.

다음과 같은 조건을 따라야 합니다:



저작자표시. 귀하는 원저작자를 표시하여야 합니다.



비영리. 귀하는 이 저작물을 영리 목적으로 이용할 수 없습니다.



변경금지. 귀하는 이 저작물을 개작, 변형 또는 가공할 수 없습니다.

- 귀하는, 이 저작물의 재이용이나 배포의 경우, 이 저작물에 적용된 이용허락조건을 명확하게 나타내어야 합니다.
- 저작권자로부터 별도의 허가를 받으면 이러한 조건들은 적용되지 않습니다.

저작권법에 따른 이용자의 권리는 위의 내용에 의하여 영향을 받지 않습니다.

이것은 [이용허락규약\(Legal Code\)](#)을 이해하기 쉽게 요약한 것입니다.

[Disclaimer](#)

이학박사 학위논문

**Manipulation of physical properties in
oxide thin films by a local inversion
symmetry breaking induced by
flexoelectricity**

변전효과에 의해 야기되는 국소적인 반전대칭
깨트림을 이용한 산화물 박막의 물성 제어

2019 년 8 월

서울대학교 대학원

물리천문학부

박성민

**Manipulation of physical properties in
oxide thin films by a local inversion
symmetry breaking induced by
flexoelectricity**

Sungmin Park

Supervised by

Professor Tae Won Noh

A Dissertation submitted to the Faculty of Seoul National
University in Partial Fulfillment of the Requirements for the
Degree of Doctor of Philosophy

June 2019

Department of Physics and Astronomy

Graduate School

Seoul National University

Abstract

The concept of symmetry plays an incredible role in physics. What kinds of symmetries the material possess determine the physical orders or properties the material can have. Depending on crystal symmetries, solid can be classified into well-known crystallographic point group. In solids, there exists 32 types of morphological crystalline symmetries derived in 1830 from a consideration of observed crystal forms. The point group of a crystal determines the directional variation of physical properties that arise from its structure, including optical properties such as birefringency, or electromechanical coupling such as piezoelectricity.

Couplings between electrical and mechanical properties are quite intriguing physical phenomena and have been used in many applications ranging from microelectromechanical systems to biological systems such as piezoelectric actuator, motor, sensor, energy generator, electromotor proteins and cellular membranes. The most popular example of electromechanical couplings is piezoelectricity in polar systems (where the space inversion symmetry is broken), in which the homogeneous strain can induce electric fields and vice versa. On the other hand, there can occur a novel electromechanical coupling known as flexoelectricity in the presence of a strain gradient (i.e., inhomogeneous strain).

The flexoelectricity can be defined as a coupling between polarization and strain gradient. One important aspect of this phenomena is that the flexoelectricity is more universal phenomena than the piezoelectricity. While piezoelectricity can arise in 20 point

groups, flexoelectricity can arise in all 32 point groups as the strain gradients itself spontaneously break the inversion symmetry. Other than that, flexoelectricity has another important aspect. Flexoelectricity become larger and larger as the scale being reduced since the strain gradient is inversely proportional to the size of sample given that the applied strain is fixed. Because of those two advantages mentioned above, flexoelectricity can play an important role in both nanoscale physics and application as it might be possible to replace the devices in which the piezoelectricity is in use.

In this thesis, I will show that it is possible to tune the physical properties of oxide thin films by breaking the space inversion symmetry induced by flexoelectricity. Specifically, I exploited the technique so called atomic force microscope (AFM) tip pressing that is applying pressure using sharp AFM tip to induce local strain gradients, thus, break the local inversion symmetry. With this technique, local control of physical properties of oxide thin films was possible and three works related to AFM tip pressing will be addressed. Our studies on oxide thin films suggest that many interesting control of local physical properties can be possible by means of pure mechanical force.

Keywords: flexoelectric, strain gradient, local inversion symmetry breaking, oxide, epitaxial thin film, polarization, AFM tip pressing.

Student number: 2014-30111

List of Figures

Figure 1.1 Schematic diagram illustrating the flexoelectric effect based on mechanical bending.

Figure 1.2 Types of strain gradients: longitudinal (a), transverse (b) and shear (c) strain gradients respectively.

Figure 1.3 Various ways of generating flexoelectricity: Macroscopic bending, Heteroepitaxial strain relaxation and AFM tip induced pressure. Adopted from Zubko et al [5], Lee et al. [8], Zubko et al. [6].

Figure 2.1 Schematic diagram of a PLD chamber.

Figure 2.2 PFM machine in CCES IBS.

Figure 2.3 PFM phase (left) and amplitude (right) images of epitaxial BiFeO₃ film.

Figure 3.1 Schematic illustration of mechanical writing of ferroelectric polarization with AFM tip pressing. Adapted from H. Lu *et al.* [3], and Y. Gu et al.[13]

Figure 3.2 Schematic display of multiple switching pathways in BiFeO₃ (BFO). Adapted from Park *et al.* [21].

Figure 3.3 Characterization of mono-domain BFO thin film. Adapted from Park *et al.* [21].

Figure 3.4 Ferroelectric polarization switching by mechanical line scan. Adapted from Park *et al.* [21].

Figure 3.5 Ferroelectric polarization switching by mechanical 2D scan. Adapted from Park *et al.* [21].

Figure 3.6 Schematic illustration of polarization switching due to the trailing flexoelectric

field tracing SPM tip motion and Phase-field modelling of IP Flexoelectric distribution under both static and mobile tip. Adapted from Park *et al.* [21].

Figure 3.7 Phase-field modelling of OP Flexoelectric distribution under both static and mobile tip. Adapted from Park *et al.* [21].

Figure 3.8 Phase-field simulation results for the case of tip motion along $[1\bar{1}0]$. Adapted from Park *et al.* [21].

Figure 3.9 Schematic illustration of polarization switching due to the trailing flexoelectric field in mechanical 2D scan. Adapted from Park *et al.* [21].

Figure 3.10 Phase-field modelling of ferroelectric switching under a mechanical load. Adapted from Park *et al.* [21].

Figure 3.11 Comparison between mechanical switching and electrical switching of ferroelectric polarization. Adapted from Park *et al.* [21].

Figure 3.12 Retention properties of mechanically switched ferroelastic domain. Adapted from Park *et al.* [21].

Figure 4.1 Colossal decrease of resistivity in highly polarized ultrathin dielectrics. Adapted from Park *et al.* [31].

Figure 4.2 Polarization-induced band crossing of STO conduction and valence bands. Adapted from Park *et al.* [31].

Figure 4.3 Schematic diagram of the potential energy profiles across polarized STO. Adapted from Park *et al.* [31].

Figure 4.4 Mechanically induced large polarization in ultrathin dielectrics. Adapted from Park *et al.* [31].

Figure 4.5 Calculated strain gradients and strains imposed by the AFM tip. Adapted from

Park *et al.* [31].

Figure 4.6 Calculated dielectric constants. Density functional theory (DFT) calculations on the total zz component of the total dielectric constant (i.e., ϵ_{zz}), which includes both ionic and electronic contributions, as a function of longitudinal strain u_{33} . Adapted from Park *et al.* [31].

Figure 4.7 Negligible strain effect in the STO bandgap. Adapted from Park *et al.* [31].

Figure 4.8 Growth and characterization of ultrathin homoepitaxial STO. Adapted from Park *et al.* [31].

Figure 4.9 Local I-V measurement setup with mechanical gating with AFM tip. Adapted from Park *et al.* [31].

Figure 4.10 Tunneling currents across a 10 unit cell-thick STO film. Adapted from Park *et al.* [31].

Figure 4.11 Colossal flexoresistance effect in ultrathin STO.. Adapted from Park *et al.* [31].

Figure 4.12 Pressure dependence of the resistivity. Although the tips with $r_{\text{tip}} = 250$ and 300 nm can generate pressure, comparable to that by the tip with $r_{\text{tip}} = 150$ nm, the resulting resistivity changes are suppressed considerably. Adapted from Park *et al.* [31].

Figure 4.13 Microscopic images of AFM tips, scanning electron microscopy images. Adapted from Park *et al.* [31].

Figure 4.14 Local I - V measurements with different dielectric materials such as BaTiO_3 and LaAlO_3 .

Figure 4.15 Colossal flexoresistance in a 10 unit cell-thick BaTiO_3 film, buffered with a graphene. Adapted from Park *et al.* [31].

Figure 4.16 Reversible flexoresistance effect. Adapted from Park *et al.* [31].

Contents

Abstract (English)	1
List of Figures	3
1. Introduction	9
1.1 Flexoelectricity	9
1.2 Types of strain gradients	10
1.3 Ways to generate strain gradients.....	12
2. Experimental detail	15
2.1 Pulsed-laser deposition	15
2.2 Piezoelectric force microscopy	17
2.3 Atomic force microscopy tip pressing for mechanical writing or gating of polarization	21
3. Trailing flexoelectric field and selective control of ferroelectric polarization in BiFeO₃ thin film	24
3.1 Mechanical switching of ferroelectric polarization	24
3.2 Trailing electric field due to the motion of the AFM tip.....	27
3.3 Mono-domain BFO thin film.....	28
3.4 Selective control of multiple ferroelectric pathways using a mechanical force induced by AFM tip pressing	31
3.5 Mechanism for selective control of multiple ferroelectric switching pathways: trailing flexoelectric field.....	35
3.6 Role of piezoelectricity and flexoelectricity in mobile AFM tip pressing studied by phase-field simulations.....	41
3.7 Comparison between trailing electric field and trailing flexoelectric field	45
3.8 Conclusion	49

4. Controlling electrical state in dielectrics with mechanical force: colossal flexoresistance	53
4.1 Introduction.....	53
4.2 Estimation of threshold polarization above which both the conduction band minimum and valance band maximum cross the Fermi level	59
4.3 Experimental results and discussion	62
4.4 Conclusion	78
5. Conclusions.....	82
Appendix A: Estimation of conversion factor between electric bias and mechanical force	84
Appendix B: Phase field simulation	87
Appendix C: First-principle caculations.....	94
Appendix D: Detailed sample characterization	99
Appendix E: Measuring nanoscale flexoelectric coefficients by mechanically tunable quantum tunneling Detailed sample characterization	102
Publication List	104
국문 초록 (Abstract in Korean)	105
감사의 글 (Acknowledgements)	107

Chapter 1

Introduction

1.1 Flexoelectricity

The flexoelectricity or flexoelectric effect is the one of the electromechanical coupling between polarization and strain gradient. In other words, if we apply the strain gradients to a material by some means, internal polarization or internal electric field will be generated inside of the material as depicted in Fig. 1.1. This effect in solids was first theoretically predicted in 1964 by Kogan [1], however, only little studies were conducted on this subject up to the end of last century. This is because the effect is expected to be very small in solids since the material will be easily destroyed before applying significant amount of strain gradients in macroscopic scale. Also, systematic control of the strain gradient by applying an external stimulus to bulk solid is challenging. Additionally, the coupling constant between polarization and strain gradient is as small as the value typically ranging from 10^{-6} C/m to 10^{-10} C/m [2,3]. However, situation could change in nanoscale. In 2011, D. Lee et al showed that the effect can be significantly enhanced at the nanoscale [4].

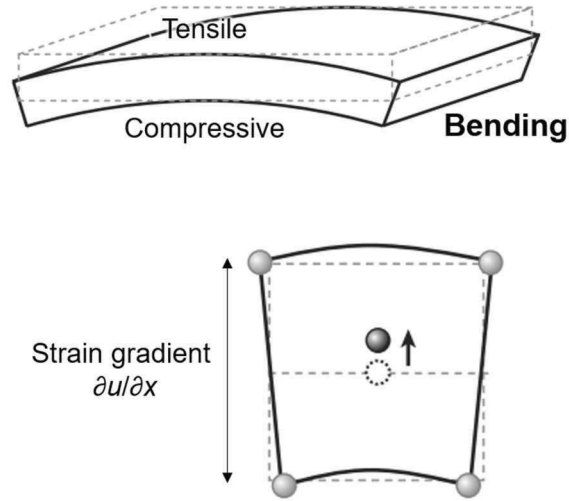


Figure 1.1 Schematic diagram illustrating the flexoelectric effect based on mechanical bending. Since the strain gradient breaks the inversion symmetry by itself, generation of electric polarization is allowed upon bending even in the centrosymmetric materials (i.e., flexoelectricity works for every dielectric material.).

1.2 Types of strain gradients

The flexoelectricity by definition is the response of electric polarization to a strain gradient thus, it must form a tensor equation. The phenomena can be expressed by the tensor relationship

$$P_l = \mu_{ijkl} \frac{\partial u_{ij}}{\partial x_k}, \quad (1.1)$$

where $P_l (E_l)$ is the generated polarization (electric field), μ_{ijkl} is the flexoelectric coefficient (a fourth-rank polar tensor), u_{ij} is a component of the elastic strain, x_k is the direction of the strain gradient.

Depending on the shape of lattice deformation, strain gradients can be classified into three or combination of them: longitudinal strain gradient, transverse strain gradient and shear strain gradient. Each types of them can be expressed as longitudinal strain gradient $\frac{\partial u_{ii}}{\partial x_i}$, transverse strain gradient consisting of $\frac{\partial u_{jj}}{\partial x_i}$ and shear strain gradient corresponding to $\frac{\partial u_{ij}}{\partial x_i}$

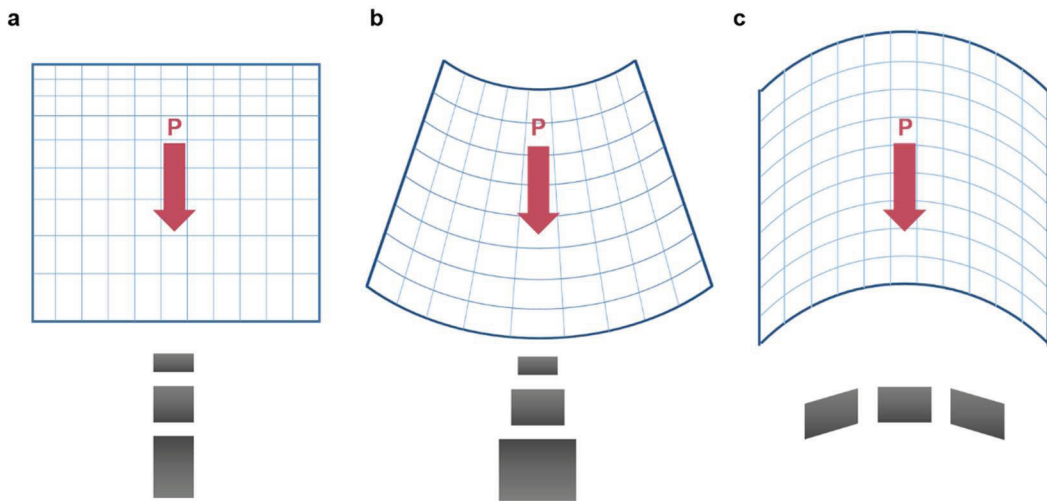


Figure 1.2 a–c, Types of strain gradients: longitudinal (a), transverse (b) and shear (c) strain gradients respectively. Red arrows indicate the direction of polarization for given strain gradients. Black squares schematically indicate the shape of unit cell distribution upon each types of stain gradients.

1.3 Ways to generate strain gradients

There are several ways to impose strain gradients in solids. First method is applying macroscopic bending to the bulk solid. Representative technique for this method is three point bending. This technique has been used for measuring bulk flexoelectric coefficient and etc [5]. Another method is exploiting strain relaxation in nanoscale thin film [4,6,7]. When a film is deposited onto the substrate with different lattice constant, at the beginning, the lattice constant of deposited materials will be matched with the one with substrate due to the substrate clamping effect. However, as the film thickness increases, film will experience strain relaxation since the original bulk state would be most stable state. Finally, there is a way to control the location and amount of strain gradients in systematic manner. By exploiting pressure applied by AFM tip, we can generate huge strain gradients locally [8-10].

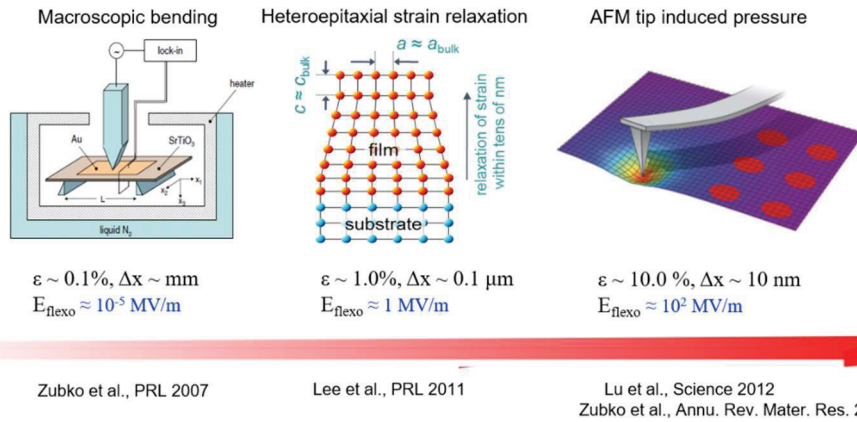


Figure 1.3 Various ways of generating flexoelectricity: Macroscopic bending, Heteroepitaxial strain relaxation and AFM tip induced pressure. Adopted from Zubko et al [5], Lee et al. [8], Zubko et al. [6].

References

- [1] Kogan, S. M. Piezoelectric effect during inhomogeneous deformation and acoustic scattering of carriers in crystals. *Sov. Phys. Solid State* **5**, 2069 (1964).
- [2] Yudin, P. V & Tagantsev, A. K. Fundamentals of flexoelectricity in solids. *Nanotechnology* **24**, 432001 (2013).
- [3] Jiang, X., Huang, W. & Zhang, S. *Nano Energy* **2**, 1079–1092 (2013).
- [4] Lee, D. et al. *Phys. Rev. Lett.* **107**, 057602 (2011).
- [5] Zubko, P., Catalan, G., Buckley, A., Welche & Scott, J. F. *Phys. Rev. Lett.* **167601**, 99–102 (2007).

-
- [6] Jeon, B. C. *et al. Adv. Mater.* **25**, 5643–5649 (2013).
- [7] Lee, D. *et al. Adv. Mater.* **26**, 5005–11 (2014).
- [8] Lu, H. *et al., Science* **336**, 59–61 (2012).
- [9] Lu, H. *et al. Nano Lett.* **16**, 6460–6466 (2016).
- [10] Guo, E. J., Roth, R., Das, S. & Dörr, K. *Appl. Phys. Lett.* **105**, 2012–2017 (2014).

Chapter 2

Experimental detail

2.1 Pulsed-laser deposition

For last several decades, lots of fabrication techniques have been developed and advanced to make high-quality thin films [1]. They include molecular beam epitaxy method, on/off-axis sputter, and pulse laser deposition (PLD) method. Among them, PLD is probably the simplest way to make a thin film with high crystalline quality [2]. PLD method offers a very wide range of deposition parameters, such as substrate temperature, oxygen partial pressure, and laser intensity. This flexibility makes the PLD method to be very attractive for investigating the effects of the deposition parameters. For example, it is known that oxide thin films have quite different physical properties, according to deposition conditions. Figure 2.1 shows a schematic diagram of a PLD chamber. It consists of a target holder and a substrate holder housed in a vacuum chamber. The substrate temperature is maintained near room temperature, in order to deposit amorphous and polycrystalline film. However, in most cases, the substrate is heated in order that its temperature is maintained at a certain temperature, high enough to deposit epitaxial film. Epitaxial growth of oxide thin films usually requires a high deposition temperature

(≥ 500 °C). A high-power laser is used as an external energy source to ablate the target material and vaporize it. And, a set of optical components is used to focus the laser beam on the target surface. The vaporization process of target material occurs by a congruent melting, and thus the chemical stoichiometry of vapor is almost the same as that of the target material. This means that we can easily make thin film with desired chemical component with PLD method.

The separation between the vacuum control equipment and the laser power source makes the PLD to be so flexible that it is easily adaptable to different operational modes. Film growth can be carried out in a reactive environment containing any kind of gases. Because of the fast and very directional plume, attenuation due to trajectory change as a result of collisions with the background gas is small.

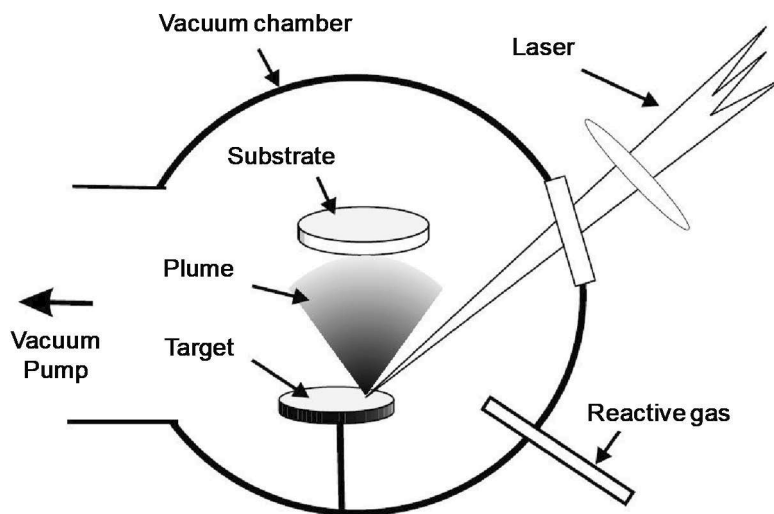


Figure 2.1 Schematic diagram of a PLD chamber. It consists of a target holder and a substrate holder housed in a vacuum chamber.

2.2 Piezoelectric force microscopy

Piezoresponse force microscopy (PFM), a specialized atomic force microscopy (AFM) technique, is a very powerful method for direct visualization of ferroelectric (FE) static domain configurations and their dynamic behaviors at nanoscale [3-7]. All FEs should exhibit the piezoelectric effect, a linear coupling between mechanical strains and electric fields. When a stress is applied to FE materials, a mechanical displacement will be induced, leading to the generation of an electric field: we call this phenomenon as piezoelectric effect. PFM detect the “*converse piezoelectric response*” of FE materials, i.e., local mechanical vibrations induced by an applied external ac field. It should be noted that PFM does not measure electrostatic signals directly, such as electrostatic force microscopy (EFM).

In conventional PFM, an ac bias, $V_{\text{tip}} = V_0 \sin \omega t$, is applied to a conductive tip of AFM in contact with a bare surface of the sample (Fig. 2.1a). Here, the amplitude of V_0 should be smaller than the coercive voltage of FE materials. Then, the local piezoelectric strain s caused by V_{tip} is that $s = s_0 \sin(\omega t + \phi)$. The amplitude s_0 and phase difference ϕ yield the information on the magnitude of piezoresponse and the orientation of polarization in FE domains, respectively. For example, as shown in Fig. 2.2, for c^- domains (polarization vector oriented normal to the surface and pointing towards the bottom electrode: called downward domains), the application of a positive tip bias results in the elongation of the sample, and piezoresponse is in-phase with the applied driving voltage, $\phi = 0$. For c^+ domains (upward domains), the resulting piezoresponse is opposite, $\phi = 180^\circ$.

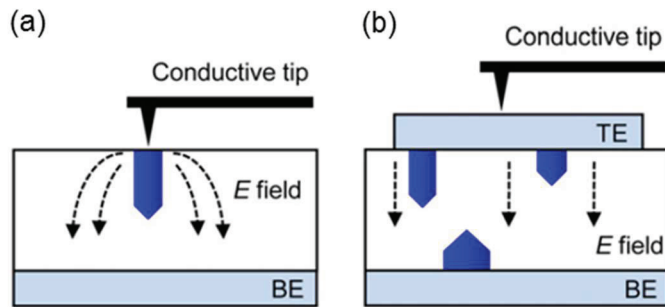


Figure 2.1 Sketch of domain nucleation (a) in conventional PFM and (b) in PFM with FE capacitor geometry. The dashed arrows indicate the electric field (denoted E field) lines. The solid needlelike (blue) figures show reversed domains (i.e., nuclei). TE and BE indicate the top and bottom electrode, respectively. Adapted from Yang *et al.* [4].

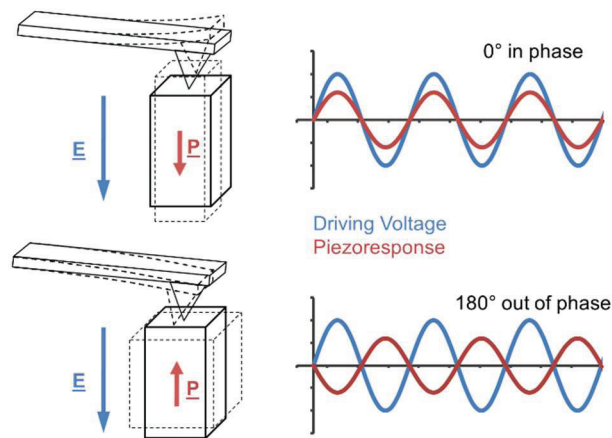


Figure 2.2 Piezoresponse of parallel (top) and antiparallel (bottom) domains. Adapted from Wikipedia [8].

The sinusoidal piezoresponse signals of s can be detected by monitoring the laser position in position sensitive photo-diode (PSPD). Using PSPD, the cantilever deflection is converted into an electrical signal and it is further processed by the AFM controller. However, typical deflections for a PFM cantilever are on the order of picometers. To increase signal-to-noise ratio, the lock-in technique is used. A dual lock-in amplifier is usually used; thus, two output signals s_0 and ϕ can be measured simultaneously, leading to both amplitude and phase PFM images. More details of conventional PFM have been published elsewhere [3-7].

It is worth noting that in the studies of real domain dynamics and statics, the domain configuration is not simple. Typically, there exist multi-domain structures with mixing upward and downward domains. In these cases, we should examine closely the contrast changes in the amplitude and phase images. The two-dimensional PFM images provide FE domain information averaged through the film along the direction of the film thickness. Figure 2.3 shows a cross-sectional schematic diagram of the FE domain switching process via nucleation, subsequent forward growth, and sideways growth of nucleated domains. At first, the nucleus appears as a small decrease only in the amplitude image. As the domain grows across the FE film, the amplitude signal decreases continuously but phase signal still does not change. After forward domain growth to half of the FE layer thickness, the phase signal changes (e.g., from 0 to 180°, and vice versa). After that, the amplitude becomes increased again. After the completion of forward domain growth, the domain wall begins to move sideways. It should be noted that at domain walls, the contribution from upward and downward domains to the piezoresponse cancel each other. As a result, the

piezoresponse at domain walls is nearly zero.

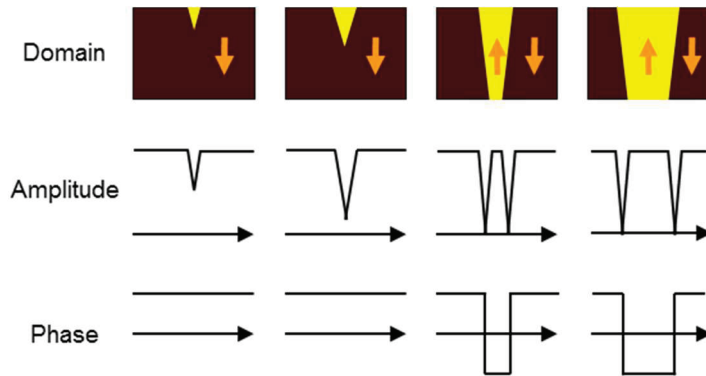


Figure 2.3 Schematics of cross-sectional amplitude and phase signals associated with domain structures in the switching process. Adapted from Yang *et al.* [9].

The conventional PFM has been used as one of most powerful tools for investigation of FE domain dynamics and statics. Nevertheless, it has several drawbacks for the domain studies (in particular, domain dynamics) occurring in real FE devices. First, although the conventional PFM provides high spatial resolution, the applied electric field is significantly dependent on the PFM tip conditions, such as tip shape, tip radius, and the relative distance between the tip and film, which are often difficult to control. Second, the applied electric field is not uniform, actually highly inhomogeneous; thus, complicated analysis should be required to estimate accurate electric field values. Third, conventional PFM can only observe local FE domain switching originating from the nucleus just below the tip (Fig. 2.1a).

2.3 AFM tip pressing for mechanical control of ferroelectric polarization

Atomic force microscope tip (AFM tip) is typically used as a nanoscale probe for various measurements ranging from surface potential, local conductivity, piezoresponse, etc. However, AFM tip can be also used as a dynamic tool to apply mechanical pressure. AFM tip has a typical dimension of few tens of nanometer and contact area of $\sim 10\text{nm}$ in contact radius. If we assume the applied force of range around $1\mu\text{N}$, then we can apply a pressure as high as few GPa. Since the contact point of a AFM tip can be regarded as a sphere, we can apply Hertz contact model to estimate strain distribution of a sample. By simple analytical model or phase field simulation, one can estimate the strain distribution of the sample, thus, the distribution of strain gradients. Given the strain gradients distribution, we can calculate flexoelectric field and developed flexoelectric field is as large as the order of $\sim 100\text{MV/m}$ which is large enough to induce ferroelectric polarization switching. The switching of ferroelectric polarization with this technique was first demonstrated by H. lu et al in 2012 [10]. When AFM tip presses the sample of upwardly polled polarization with mechanical force, it will deform the pressed region, thus, generating downward flexoelectric field. If the generated flexoelectric field is larger than the coercive field of the ferroelectric film, then polarization will be switched to downward direction as depicted in Fig 1.1 and 1.3. Experimental procedure for mechanical writing of ferroelectric polarization is as follow. First, target region needs to be polled with electric bias so that the direction of the polarization to be upward since the direction of the

flexoelectric field is downward. After that, scan the target region with pressure applied by AFM tip to switch the polarization. To confirm the switching, conduct the PFM measurement.

References

- [1] H. Kitahata, K. Tadanaga, T. Minami, N. Fujimura, and T. Ito, *Jpn. J. Appl. Phys.* **38**, 5448 (1999).
- [2] D. B. Chrisey and G. K. Hubler, eds., *Pulsed laser deposition of thin films*, John Wiley & Sons, Inc., 1994.
- [3] M. Alexe and A. Gruverman, *Ferroelectrics at Nanoscale: Scanning Probe Microscopy Approach* (Springer, New York, 2004).
- [4] S. M. Yang, J.-G. Yoon, and T. W. Noh, *Curr. Appl. Phys.* **11**, 1111 (2011).
- [5] A. Gruverman, O. Auciello, and H. Tokumoto, *Annu. Rev. Mater. Sci.* **28**, 101 (1998).
- [6] S. Hong *et al.*, *J. Appl. Phys.* **89**, 1377 (2001).
- [7] S. V. Kalinin and D. A. Bonnell, *Phys. Rev. B* **65**, 125408 (2002).
- [8] http://en.wikipedia.org/wiki/Piezoresponse_force_microscopy.
- [9] S. M. Yang, T. H. Kim, J.-G. Yoon, and T. W. Noh, *Adv. Funct. Mater.* **22**, 2310 (2012).
- [10] Lu, H. *et al. Science* **336**, 59–61 (2012).

Chapter 3

Trailing flexoelectric field and selective control of ferroelectric polarization in BiFeO₃ thin film.

3.1 Mechanical switching of ferroelectric polarization

Flexoelectricity refers to an electromechanical coupling between electrical polarization and strain gradient [1], allowing pure mechanical control of electrical polarization without applying an electrical stimulus [2,3]. Recently, nanoscale flexoelectricity has attracted substantial attention as an effective alternative tool for switching electrical polarization [3-6] and constructing nanoelectromechanical devices [7,8]. In fact, flexoelectricity was revealed and theoretically demonstrated around fifty years ago [1]. For a long time, its effects in bulk solids had been believed to be negligible, since these materials normally experience crack-mediated structural breakdowns before huge strain gradients develop. Only recently, it has been reported that the flexoelectric effects can become dramatically enhanced at the nanoscale inside epitaxial oxide films [9-12]. Furthermore, the flexoelectricity was directly demonstrated by mechanically switching the ferroelectric polarization of a uniaxial system, such as compressively-strained BaTiO₃ thin films (Fig. 3.1 a-c), without any usage of electric bias through an electrically grounded AFM tip [3,6].

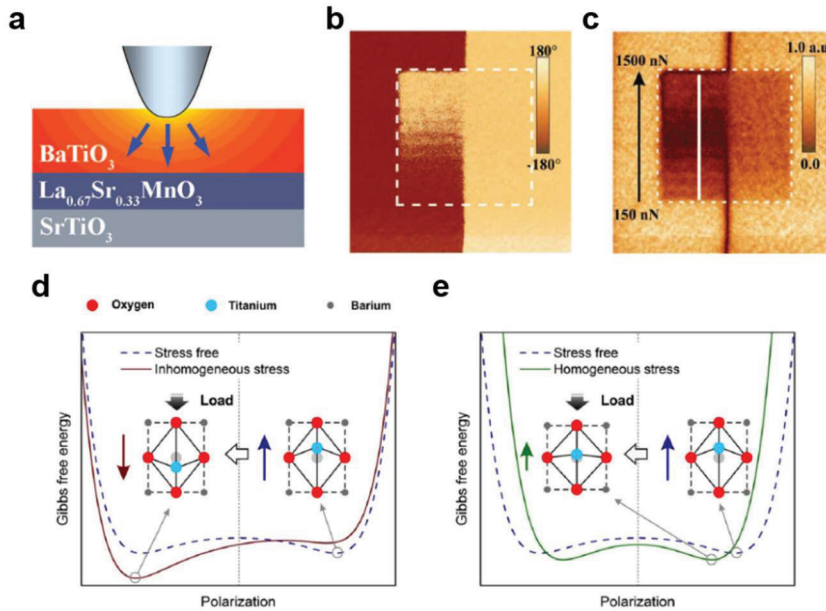


Figure 3.1 a, Schematic illustration of mechanical writing of ferroelectric polarization with AFM tip pressing. The blue arrows indicate the generated flexoelectric field. b,c, Out of plane PFM phase image (b) and amplitude image (c) after the application of incremental loading force from 150 to 1500nN on upwardly poled BaTiO₃ film with AFM tip. d,e The free energy profile change in the case of flexoelectric coupling (d) and piezoelectric coupling (e). Adapted from H. Lu *et al.* [3], and Y. Gu *et al.*[21]

The mechanism of ferroelectric polarization by mechanical stimulus can be easily understood if we recall the free energy diagram of ferroelectric materials. Typical c-axis oriented displacive ferroelectric materials such as BaTiO₃ and PbTiO₃ possess double-well-shaped free energy profile (Fig. 3.1. d,e). Depending on whether applied stress due to the mechanical loading is homogeneous or inhomogeneous, the resulted variation on the shape of free energy profile will be changed significantly. While homogeneous stress changes only the value of polarization, inhomogeneous stress can change the direction as well as the value of

polarization. For the case of AFM tip pressing on upwardly polled ferroelectric materials, since the generated flexoelectric field is downward in OP direction, corresponding free energy profile would be tilted and only the downward polarization becomes the stable state. Thus, observed ferroelectric polarization switching by AFM tip pressing is a flexoelectric origin.

Mechanical control of ferroelectric polarization has many advantageous features compared with electrical approach. For examples, mechanical control avoids applying a voltage to a thin film and thus removes problems of leakage, breakdown caused by extrinsic effect such as Joule heating. It also removes the need for a bottom electrode for a construction of device. However, there is a serious drawback for this approach with conventional c-axis oriented ferroelectric materials. Since the direction of flexoelectric field is always downward when it comes to AFM tip pressing, operation can be only unidirectional (i.e. only the switching of upward polarization is possible).

3.2 trailing electric field due to the motion of the AFM tip

The lateral motion of a biased AFM tip can effectively break the rotational symmetry of a generated electric field distribution inside the film [14]. When the positively (negatively) biased tip moves, the electric field acting on the domain switching at last becomes generated in the direction antiparallel (parallel) to the tip motion. This effect can be denoted effectively as an in-plane (IP) electric field in the region trailing the SPM tip motion, so named as “trailing electric field” [15,16]. Such trailing field has been widely utilized for manipulating nanoscale ferroelectric domains of low-symmetry multiaxial ferroelectrics such as BiFeO₃ (BFO) in recent years [14,17,18]. For example, Nina Balke *et al* selected specific polarization variants by controlling scan direction and could generate vortex and anti-vortex domain structures in multiferroic BFO film. However, the mechanical version of the trailing field and its role on the domain engineering had not been investigated properly before this work.

3.3 Mono-domain BFO thin film

To facilitate the trailing IP flexoelectric field for mechanical switching of ferroelectric polarization, we chose BFO as a model system as it has both OP and IP polarization components. In multiferroic BFO with the polarization pointing

along the pseudocubic $\langle 111 \rangle$, there are three possible domain switching pathways which are the 71° , 109° , and 180° switching, as schematically illustrated in Fig. 3.2. Between them, 71° and 109° switching also accompany change of the direction of lattice distortion, thus change in crystal structure (i.e., ferroelastic switching), leading to the reorientation of antiferromagnetic spin configuration. This indicates that such ferroelastic switching pathways can be used for novel magnetoelectric devices [19,20].

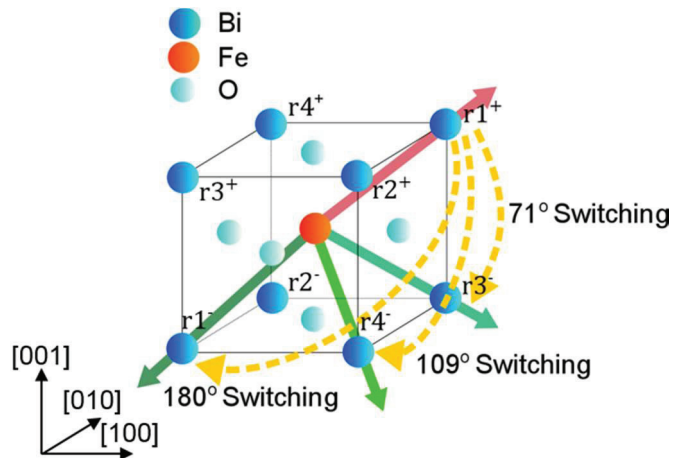


Figure 3.2 Schematic display of multiple switching pathways in BiFeO₃ (BFO). Each straight arrow indicates the direction of the polarization, and each yellow dashed arrow indicates the three possible switching pathways, respectively. Adapted from Park *et al.* [21].

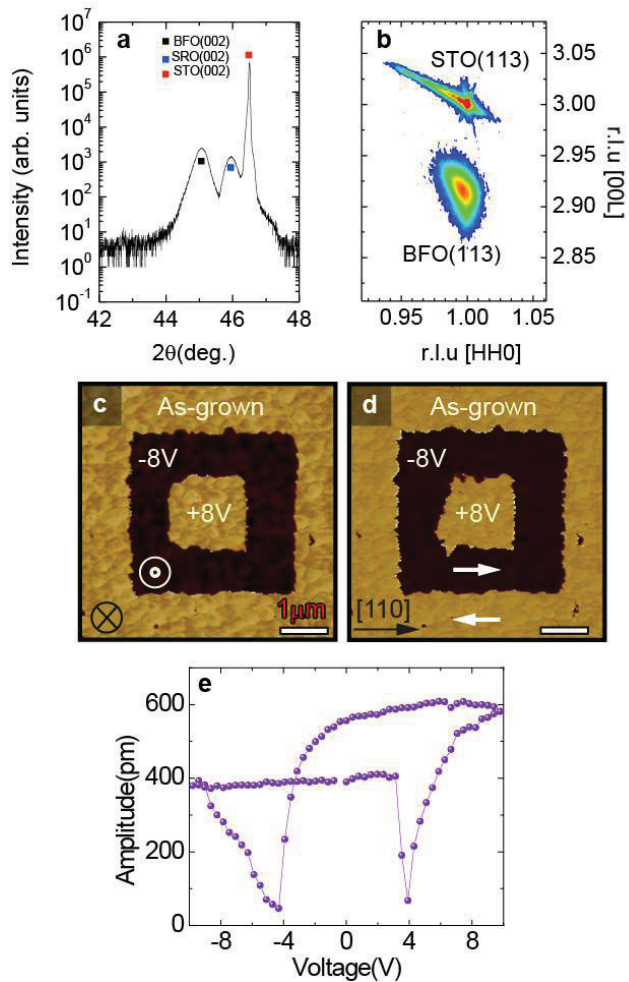


Figure 3.3 Characterization of mono-domain BFO thin film. **a**, X-ray diffraction θ - 2θ scan of the 100-nm-thick BFO film buffered by SrRuO₃ bottom electrode grown on vicinal SrTiO₃ (001) substrate with 4° miscut angle along [110] direction. **b**, Reciprocal space mapping near (113) SrTiO₃ diffraction. **c–e**, The corresponding out-of-plane (OP) (**c**) and in-plane (IP) (**d**) piezoresponse force microscopy (PFM) phase images and PFM hysteresis loop (**e**). Adapted from Park *et al.* [21].

For the reasons mentioned in above paragraph, we fabricated 100-nm-thick BFO films on top of a bottom electrode SrRuO₃ layer using pulsed laser deposition technique introduced in Chapter 2. The films were deposited on a vicinal SrTiO₃

(100) substrate with 4° miscut along the [110] direction. The choice of this substrate miscut enables us to simplify the system for studying mechanical switching of ferroelectric polarization because it allows stabilization of the mono-domain state in the as-grown films (i.e. possessing only one structural variant) [22]. Detailed condition for the sample deposition is as follow. First, atomically flat TiO_2 terminated SrTiO_3 substrates were prepared by HF etching and annealing. After that both BFO film and SrRuO_3 layer were deposited on it. Deposition temperatures of BFO and SrRuO_3 were 640°C and 700°C , respectively and both layers were grown at an oxygen partial pressure of 100 mTorr. The laser repetition frequency and energy were set to 2 Hz with 1.5 J cm^{-2} for SrRuO_3 layer and 5 Hz with 1.5 J cm^{-2} for BFO layer. After deposition, the sample was cooled to room temperature in an oxygen environment at 760 mTorr, at a rate of $10^\circ\text{C min}^{-1}$.

After the sample fabrications, basic characterization such as PFM and X-ray diffraction measurements were conducted to confirm the initial states of the polarization distribution in as-grown samples. All of our BFO films had only the $r1^-$ domain (polarization pointing towards $[11\bar{1}]$, please see the Fig. 3.2 to understand the notation for each polarization variants) in the as-grown state, verified by X-ray reciprocal space mapping and basic PFM characterizations (Fig. 3.3).

3.4 Selective control of multiple ferroelectric pathways using a mechanical force induced by AFM pressing in BFO film

We performed a series of experiments to induce the selective domain switching by AFM tip pressing. Note that the AFM tip-induced OP flexoelectric field direction points downwards only [3]. Since the as-grown domain in our BFO film is only composed of $r1^-$, we initially poled the domain to $r1^+$ by applying an electric bias of -7 V through AFM tip/BFO/SrRuO₃ junction. Then, without application of any electric bias, we applied a constant loading force of 5 μ N by an electrically grounded tip and conducted a one-dimensional (1D) line scan (referred to as “mechanical scan” hereinafter). Figure 3.4 shows a typical rectangular spiral pattern used in the study (Fig. 3.4 a). The background image indicates topography of the scanned region. (Note that no topography change was detected between before and after the mechanical scan.) After the mechanical scan, we conducted a PFM imaging to determine the resultant polarization configuration. For PFM imaging, we used a small loading force of 0.25 μ N to avoid further unintentional domain switching.

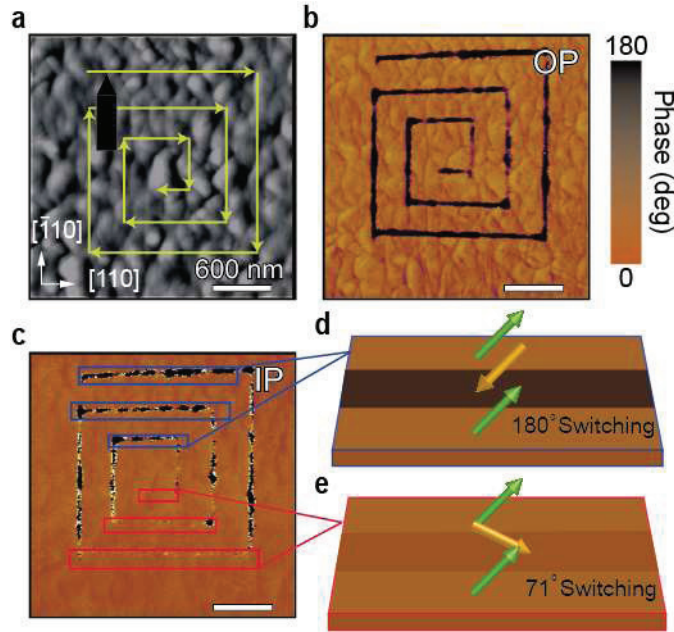


Figure 3.4 Ferroelectric polarization switching by mechanical line scan. a, Schematic of our mechanical line scan and topography image of the scanned region. Yellow arrows indicate the direction of tip movement. b,c, The OP (b) and IP (c) PFM phase images after mechanical scan performed on the BFO thin film. The scale bars are 600 nm. (d,e). Schematic display of polarization configuration after mechanical scan. d, 180° switching for scan along $[110]$ direction and e, 71° switching for scan along $[\bar{1}10]$ direction in BFO film. Mechanical scan was performed with a fixed contact force of $5 \mu\text{N}$. Before the scan, a $3 \times 3 \mu\text{m}^2$ area was poled with -7 V of tip bias to ensure a uniform initial polarization to $r1^+$. The scan was performed parallel and normal to the $[110]$ direction. Adapted from Park *et al.* [21].

In Fig. 3.4b, the OP PFM phase image displays the phase contrast change of $\sim 180^\circ$ in mechanically scanned region, indicating the OP polarization switching was nothing to do with the scanning direction. However, the IP PFM phase image presents different contrasts which were dependent on the scanning direction (Fig. 3.4c). For the case of mechanical scan along $[110]$ direction, both OP and IP phase

contrasts change indicating 180° switching (Fig. 3.4d). On the other hand, when the mechanical scan was along $[\bar{1}\bar{1}0]$ direction, only the OP phase contrast changes and IP phase contrast seems to be barely affected, indicating 71° switching (Fig. 3.4e). Under mechanical scan along other directions, namely $[\bar{1}10]$ and $[1\bar{1}0]$, complex mixtures of 180° and 71° switchings are observed. This is ascribed to the instability of the 109° domain wall and the subsequent relaxation into the 180° and 71° domains. These PFM results demonstrate the validity of mechanical control of multiple ferroelectric switching pathways with AFM tip pressing.

We also tried typical 2D area scans. Figure 3.5 shows the IP PFM images after 2D mechanical scans with different scan angles over the $3 \times 3 \mu\text{m}^2$ areas of the initially upwardly switched ($r1^+$) region. The scan angle during the 2D mechanical scans were sequentially changed from 0° to 180° with increment angle of 45° . Note that the scan angle of 0° (180°) refers to the direction of slow scan axis being antiparallel (parallel) to the substrate miscut direction $[110]$. For all scan angles, the OP PFM phase changes, indicating switching of the polarization in OP direction (insets of Fig. 3.5). However, the IP PFM phase images reveal a gradual variation of phase contrast from 0° (yellow) to mixed and finally 180° (black) depending on the scan angle. By accounting both the OP and IP PFM phase images, we made the conclusion that 71° switching ($r1^+ \rightarrow r3^-$) and 180° switching ($r1^+ \rightarrow r1^-$) occurred for the case of 0° and 180° scan angles, respectively. For intermediate scan angles (45° , 90° , and 135°), a mixture of $r1^-$ and $r3^-$ domains was formed similar to the

case of 1D mechanical scan. Moreover, for intermediate scan angles (45°, 90°, and 135°), the portion of the $r1^-$ and $r3^-$ domains was systematically changed as the scan angle increases. The mechanism of observed experimental results will be discussed in next section.

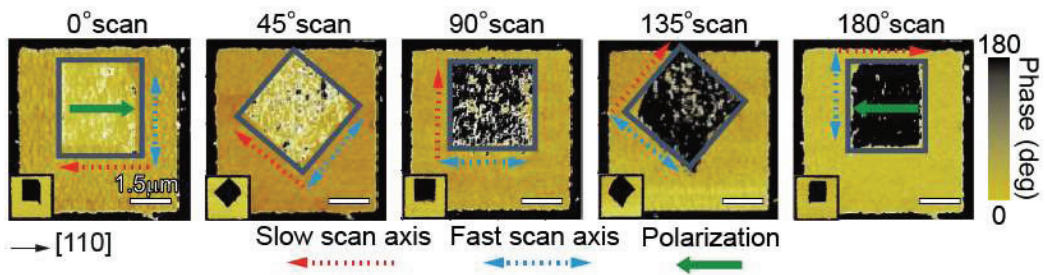


Figure 3.5 Ferroelectric polarization switching by mechanical 2D scan. IP PFM phase images with scan angles of 0°, 45°, 90°, 135° and 180° after switching a distinct $3 \times 3 \mu\text{m}^2$ upwardly pre-poled region with a contact force of $5 \mu\text{N}$. The yellow square surrounded by the black region was initially polled with -7 V . The red and blue dotted arrows indicate the direction of the slow scan axis and the fast scan axis, respectively. Insets: The corresponding OP PFM phase images. The scale bars are $1.5 \mu\text{m}$. Adapted from Park *et al.* [21].

3.5 Mechanism for selective control of multiple ferroelectric pathways: trailing flexoelectric field

We introduce the concept of ‘trailing flexoelectric field’ which is the effective flexoelectric field trailing an electrically grounded APM tip with a high loading force, similar to its electrical counterpart [15,16]. Since the tip is electrically neutral, the field only come from the strain gradient beneath the tip by flexoelectricity. This flexoelectric field would be rotationally symmetric for the case of simple pressing without tip motion (Fig. 3.6a). When this trailing flexoelectric field is sufficient for domain nucleation, it would allow selective control of the $r1^+$ domain into either the $r1^-$ or the $r3^-$ domain by manipulating the scan direction as in 1D mechanical scan (Fig. 3.6b,c). Besides, in the trailing flexoelectric case, friction between the tip and the sample surface would create additional shear strain gradients and it can induce rotational asymmetry in generated flexoelectric field, in contrast to its electrical counterpart. Such asymmetry could be supportive in deterministic selection of domain switching pathways in BFO film.

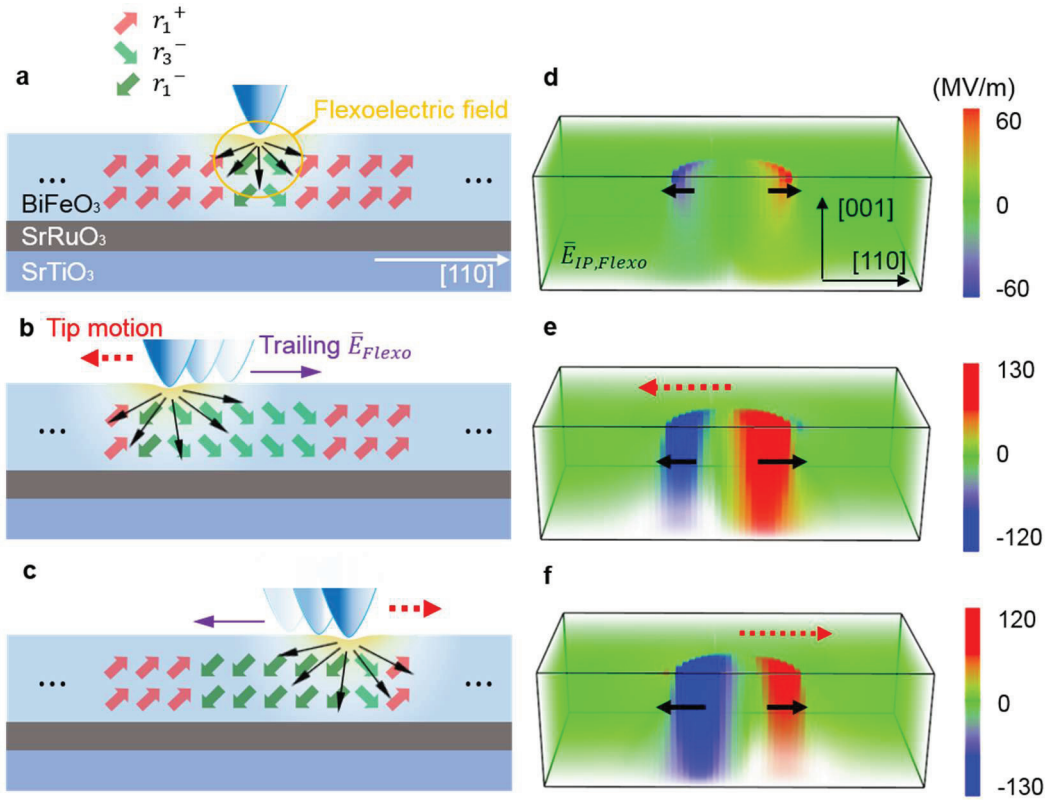


Figure 3.6 Schematic illustration of polarization switching due to the trailing flexoelectric field tracing SPM tip motion and Phase-field modelling of IP Flexoelectric distribution under both static and mobile tip. a–c, Schematic sketches of the flexoelectric field and corresponding polarization switching in a BFO film under a scanning probe in (a) static contact, tip motion along (b) $[\bar{1}\bar{1}0]$ and (c) $[110]$ directions, respectively. d–f, IP flexoelectric field distribution in a BFO film under a scanning probe in (d) static contact, tip motion along (e) $[\bar{1}\bar{1}0]$ and (f) $[110]$ directions. A constant normal force of $5 \mu\text{N}$ was applied by the tip in all simulation cases of the IP flexoelectric field distribution. Adapted from Park *et al.* [21].

Furthermore, with aid of phase field simulation, we have simulated the both IP and OP flexoelectric field distributions with the static loading force of $5 \mu\text{N}$ (i.e., simple pressing) and with tip motion along the $[\bar{1}\bar{1}0]$ direction, and that along the $[110]$ direction as depicted in Figure 3.6d–f and Figure 3.7a–c. It can be seen that

the maximum of downward OP flexoelectric field is located beneath the center of the contact region, whereas the maximum for the IP flexoelectric field is formed around the contact edges. In particular, for the case of tip motion, the IP flexoelectric field distribution indeed becomes spatially asymmetric as the volume of each positive (bluish region) and negative (reddish region) IP field distribution expands compared to the static pressing case. In addition, the maximum value of the IP flexoelectric field escalated by almost 100% compared to the static tip pressing case. The simulation results also reveal that the IP flexoelectric field can be comparable to (even higher than) the OP flexoelectric field. This suggests that the IP flexoelectric field can play a crucial role in BFO domain switching with AFM tip pressing.

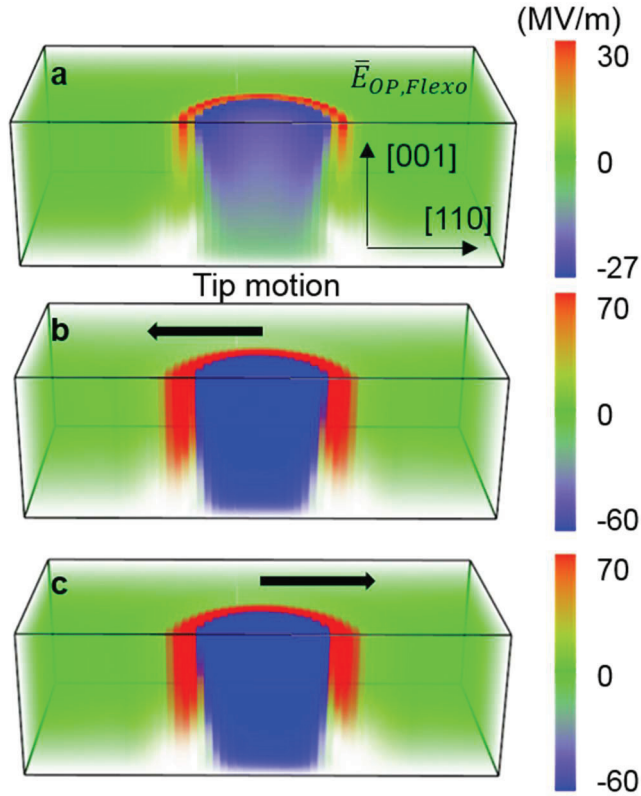


Figure 3.7 Phase-field modelling of OP Flexoelectric distribution under both static and mobile tip. a–c, OP flexoelectric field distribution under static load (a), tip motion along $[\bar{1}10]$ (b) and tip motion along $[110]$ (c) direction. Adapted from Park *et al.* [21].

Now, let us recall the experimental results (Fig. 3.4). for the case of mechanical 1D scan along either $[110]$ or $[\bar{1}\bar{1}0]$ indeed resulted IP polarization is along the direction opposite to tip motion. However, the scan along $[1\bar{1}0]$ or $[\bar{1}10]$ showed switching pathways of both 71° switching and 180° switching which are inconsistent to the direction of trailing flexoelectric field (desirable switching pathway is 109° switching). We also rationalized this inconsistency by performing

phase-field simulation on polarization evolution when the tip scans along $[1\bar{1}0]$ and $[\bar{1}10]$ directions. The resulting polarization configurations under mechanical load and the relaxation process after removing the loading force are shown in Figure 3.8 for $[1\bar{1}0]$ scanning while the results of $[\bar{1}10]$ scanning just mirror the former (not shown here).

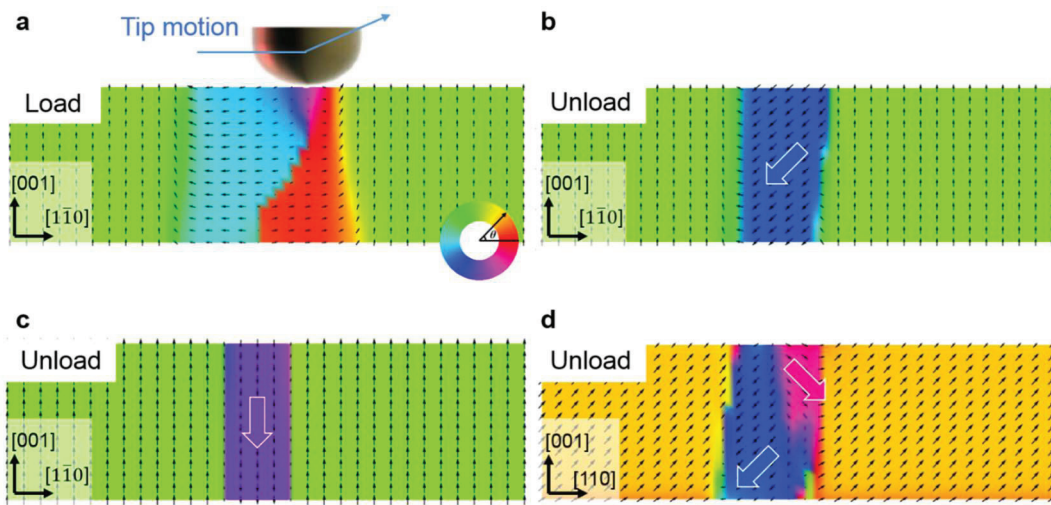


Figure 3.8 Phase-field simulation results for the case of tip motion along $[1\bar{1}0]$. a–d, Simulated polarization configurations under moving contact load along $[1\bar{1}0]$ (a) and after 1000 time steps (b), 5000 time steps (c and d) from the time when the load is released. The section view of polarization distribution normal to (110) plane (a-c) and normal to $(\bar{1}\bar{1}0)$ plane (d). The colors for the polarization configuration in each figures indicate the direction of the polarization vectors according to the polarization wheel presented in a. The vertical dimension in polarization vector maps has been expanded by factor of 4 for the clearer illustration of the polarization vectors. Adapted from Park *et al.* [21].

The simulation results confirm that the 109° switching indeed occurs under the AFM tip pressing where polarization rotates along the direction of trailing flexoelectric field (Fig. 3.8a,b), in agreement with our argument that the direction

of trailing flexoelectric field governs the switching pathway. However, the resulting 109° domain walls reside within (110) planes, which is highly unstable because of the elastic and electric incompatibility [23]. Consequently, the domain resulting from 109° switching becomes relaxed into a mixture of $r1^-$ or $r3^-$ in the process (Fig. 3.8c,d) and finally into completely $r1^-$ (180° switching) due to the release of elastic energy. It should be noted that kinetic effects such as point defects may serve as the pinning center in real experiments, thus stabilizing the mixed state (Fig. 3.4 and Fig.3.5) which is not thermodynamically stable in the phase-field simulations.

Finally, we explained the direction of trailing flexoelectric field in 2D mechanical scan case (Fig. 3.9). While the direction of trailing flexoelectric field is along the opposite direction of the scanning direction in 1D scan, the direction of trailing flexoelectric field is along the direction opposite to the slow scan axis in 2D scan. Final domain formation is mostly determined by the last flexoelectric field experienced by the domain, which is the definition of the trailing flexoelectric field, and it is perpendicular to the scanning direction (direction of fast scan axis). Based on these results, we demonstrated that the trailing flexoelectric field aligns anti-parallel to the direction of slow scan axis for the 2D mechanical scan, which is in agreement with the trailing electric field case[15-18].

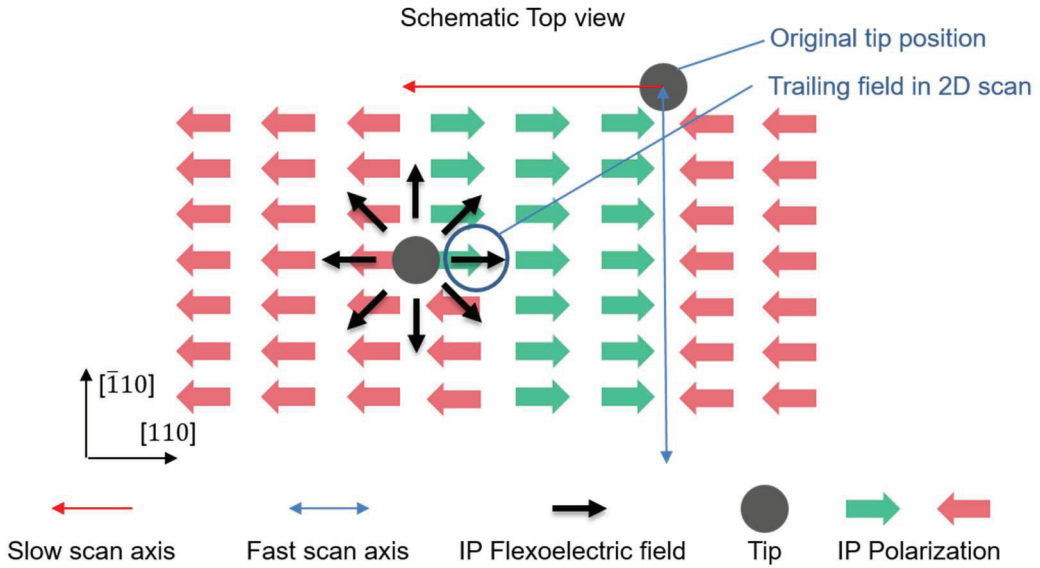


Figure 3.9 Schematic illustration of polarization switching due to the trailing flexoelectric field in mechanical 2D scan. The direction of trailing flexoelectric field in 2D mechanical scan is along the direction opposite to the slow scan axis. Adapted from Park *et al.* [21].

3.6 Role of piezoelectricity and flexoelectricity in mobile AFM tip pressing studied by phase-field simulations

Since BFO is ferroelastic material, the direction of polarization is coupled with a direction of lattice distortion. Thus, frictional shear stress could induce ferroelastic 71° switching via piezoelectricity for the case of tip motion along $[\bar{1}\bar{1}0]$ direction. To differentiate the role of piezoelectricity and flexoelectricity, we performed phase-field simulations for AFM tip scanning along the $[\bar{1}\bar{1}0]$ and the $[110]$ directions. One of the advantage of the phase-field simulation is that we can turn on and off some components such as flexoelectricity by setting a coefficient to

be zero or not.

Fig. 3.10 shows the polarization configuration under mechanical loading of $5\mu\text{N}$ by an AFM tip when flexoelectricity is considered (Fig. 3.10a,b). When the tip presses the film, the domain beneath the tip is switched by the flexoelectric field (similar to Fig. 3.6a), forming a distinct domain wall (the dotted lines in Fig. 3.10a,b); as the tip moves, this domain wall becomes slanted towards the tip motion direction. Interestingly, the polarizations continuously rotate to satisfy the head-to-tail condition in the other switched regions. This indicates that the domains prefer to lower the electrostatic energy cost.

In the trailing regions specifically, (i.e., the reddish region in Fig. 3.10a, and bluish region in Fig. 3.10b) the polarizations point towards the opposite direction to the tip motion and have mainly in-plane components; specifically, the reddish and bluish regions have predominantly $[110]$ and $[\bar{1}\bar{1}0]$ polarizations, respectively. After unloading the AFM tip, these polarizations are not allowed in terms of structural variants; namely, the polarization should point only towards one of eight possible polarization directions. Thus, they would relax to $r3^-$ domain and $r1^-$, which are the most closest allowed polarization directions, when the tip is unloaded. This simulation results explain the experimental observations well, indicating that the trailing flexoelectric field plays a critical role in domain selection, i.e., either purely $r1^-$ or $r3^-$ in the BFO film.

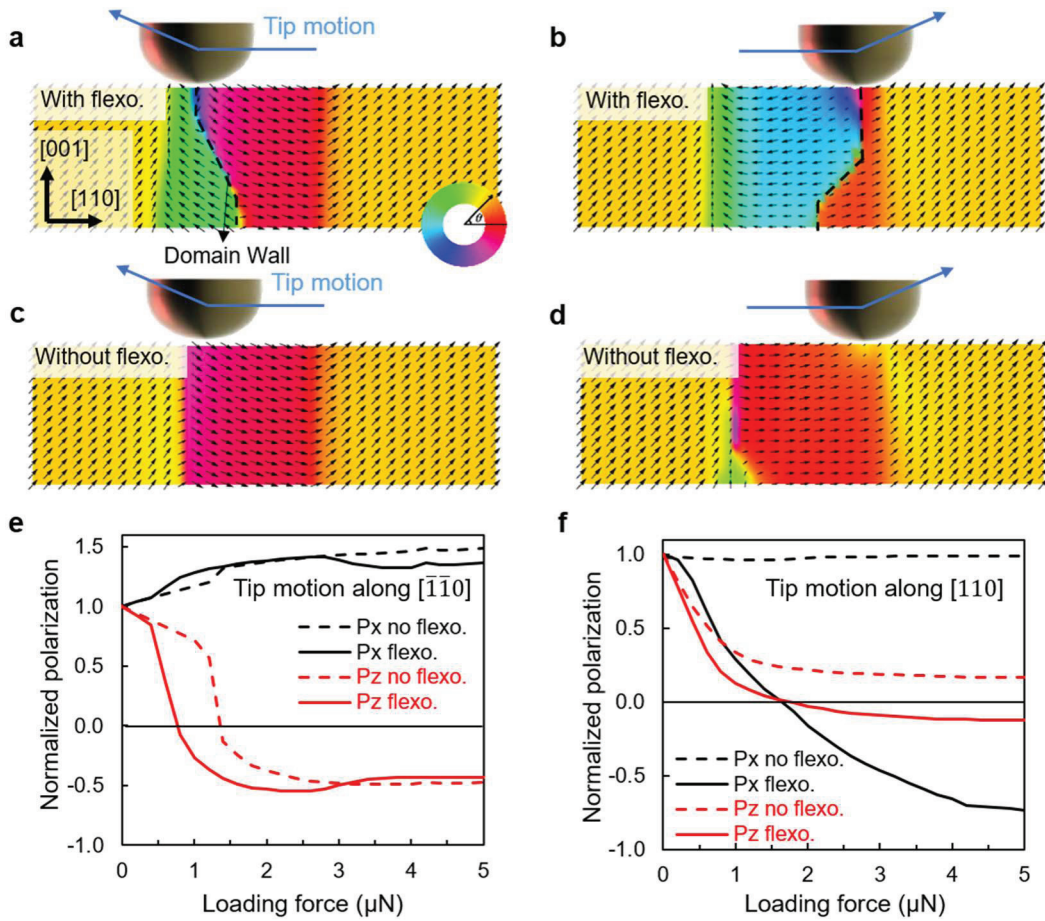


Figure 3.10 Phase-field modelling of ferroelectric switching under a mechanical load. **a,b**, Polarization configuration under mechanical loading by a SPM tip in a lateral motion along the $[\bar{1}\bar{1}0]$ (a) and $[110]$ (b) directions with a contact force of $5 \mu\text{N}$. **c,d**, Same as a and b, but without considering the flexoelectric effect. The colours for the polarization configuration in each figure indicate the direction of the polarization vectors according to the polarization wheel presented in a. **e,f**, The IP polarization P_x (black) and OP polarization P_z (red) as a function of loading forces with tip motion along $[\bar{1}\bar{1}0]$ (e) and $[110]$ (f) directions. The vertical dimension in the polarization vector maps is expanded by a factor of four to provide a clearer illustration of the polarization vectors. Adapted from Park *et al.* [21].

For the case of without flexoelectricity, we intentionally set all flexoelectric

coefficients to zero and replicated the same simulations to illustrate the key role of the flexoelectricity (Fig. 3.10c,d). Although this is a physically unrealistic, it can provide deeper insight into the separation of the role of flexoelectricity and piezoelectricity respectively. We observed that ferroelastic 71° switching ($r1^+ \rightarrow r3^-$) can be realized in this case due to the ferroelastic switching due to the piezoelectricity when the tip motion is along $[\bar{1}\bar{1}0]$ direction (Fig. 3.10c). However, ferroelectric 180° switching ($r1^+ \rightarrow r1^-$) cannot be achieved without a flexoelectric contribution (Fig. 3.10d) as the tip motion along $[110]$ direction would not change the direction of the structure distortion. This stresses again that the flexoelectric effect is essential to explain experimentally observed selective control of BFO domains.

Although the 71° ferroelastic switching could occur in the absence of flexoelectricity, the enhancing role of flexoelectricity on 71° switching is revealed in Fig. 3.10e in that the critical force for the 71° ferroelastic switching. The intercept point of P_z with x axis in solid line is significantly reduced to $\sim 0.7 \mu\text{N}$ compared with the one with dotted line which is $\sim 1.4 \mu\text{N}$, because of the contribution from flexoelectric effect. More importantly, ferroelectric 180° switching ($r1^+ \rightarrow r1^-$) cannot be achieved without a flexoelectric contribution as there is no intercept of P_z with x axis in dotted line (Fig. 3.10f). This results stresses again the essential role of the flexoelectric effect for selective control of BFO domains.

3.7 Comparison between trailing electric field and trailing flexoelectric field

Finally, we demonstrate the superiority of the trailing flexoelectric field over the trailing electric field in the context of selectivity of domain switching pathways. For this comparison, we performed mechanical and electrical scans over an initially upwardly poled domain. The upper panel was PFM phase image written by applying 5 μN of contact force and the lower panel by 7 V of electric bias. The left and right panels were scanned by setting the scan angle to 180° and 0° , i.e., the slow scan directions were $[110]$ and $[\bar{1}\bar{1}0]$ for the former and later cases, respectively (Fig. 3.11a). Interestingly, 71° switching was only possible with mechanical forces. Regions with electrical biases show 180° switching regardless of the scan direction while regions with mechanical loads display two different monodomain states in the IP PFM phase image.

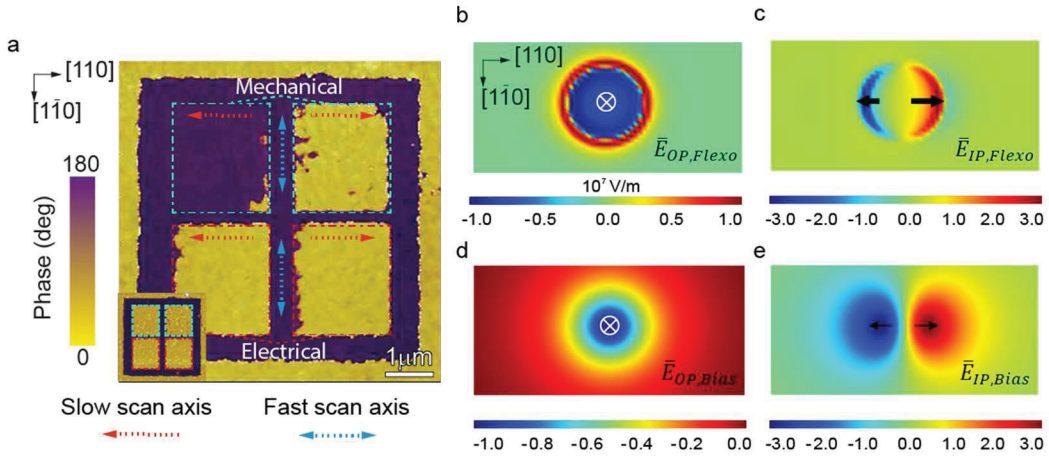


Figure 3.11 Comparison between mechanical switching and electrical switching of ferroelectric polarization. a Comparison between mechanical and electrical switching. Upper two squares were written by applying 5 μ N force and bottom two by 7 V of electric bias. b,c, Distribution of flexoelectric field in OP (b) and IP (c) direction by application mechanical force when tip motion is along $[\bar{1}\bar{1}0]$ direction. d,e, Distribution of electric field in OP (d) and IP (e) direction by application of electric bias. Both electric field and flexoelectric field are simulated by scaling the IP electrical field and IP flexoelectric field to their corresponding OP components which are aligned with same peak values for qualitative comparison as written in the manuscript. Adapted from Park *et al.* [21].

To achieve non-180° switching, the ability to impart large IP field is an important factor. In this context, we performed phase-field simulations and compared the field distribution between electrical field generated by the 3V biased tip and the flexoelectric field induced by the 3.3 μ N force-loaded tip on the film, accounting the mechanical-electrical conversion factor [24] estimated from experiments (Appendix A). Since the magnitude and distribution of fields are highly dependent on the chosen parameters such as tip shape and radius, only a qualitative comparison is possible by scaling the IP components of the electrical

field and flexoelectric field to their respective OP counterparts. For the mechanical loading case, the magnitude of the maximum IP flexoelectric field is larger than the one with OP flexoelectric field (Fig 3.11b,c). For the electrical bias case, however, the magnitude of the maximum IP electric field is much smaller than that of the OP electric field (Fig. 3.11d,e). We argue that IP electric field induced by the electric bias is not large enough to influence on the IP polarization switching, for the case of OP electric field similar to the coercive voltage of OP polarization switching, therefore accounting for the absence of 71° ferroelastic switching under the electrical stimuli. Also, for the electric switching case, applied force is as little as $0.25\mu\text{N}$, hence piezoelectric effect cannot assist 71° ferroelastic switching unlike mechanical case.

In addition, the mechanically 71° switched domain shows a decent retention property, in other words, there was almost no back switching (Fig. 3.12). As can be inferred from OP amplitude image in Fig. 3.12, the written domains were completely switched and they were steady over 12h and more (i.e., PFM amplitude shows same value in switched region and initially electrically polled region). Stability of the switched domain is essential for realizing novel devices. Mechanical switching show advantage compared with electrical switching in terms of the retention property. Because it is known that electric bias driven 71° domain switching is subjected to ferroelastic relaxation. To avoid the unwanted relaxation process, it requires further laborious process, such as the fabrication of nano-islands

to discharge the accumulated elastic stress [19]. Though, we do not exactly understand the reason for the enhanced stability of mechanically switched ferroelastic domain ($r3^-$) unlike the case switched by electric field, there are several possible explanations. The energy landscape for the polarization switching in BFO could be not same between electrical switching and mechanical switching due to the generation of much higher IP field and/or direct ferroelastic switching by mechanical stress from complementary piezoelectric effect. However, the exact origin of this observation requires further study.

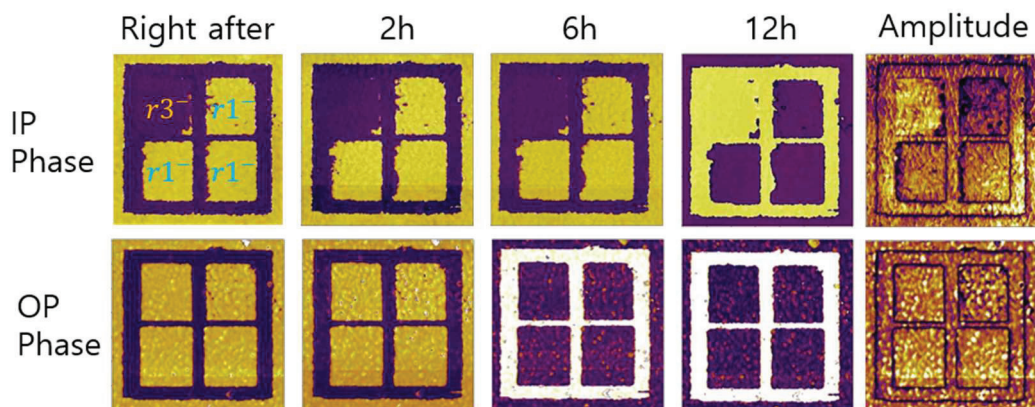


Figure 3.12 Retention property of mechanically written ferroelastic domain. First 4 images in upper panel are the IP PFM images obtained at different times after mechanical switching experiment and first 4 images in bottom panel are corresponding OP PFM images. Each 4 small squares were scanned in the same way as described in figure 5 in main text. Contrast inversion in IP phase image of 12h, OP phase image of 6h and 12h are PFM measurement artifact. Amplitude images in the last column corresponds to the amplitude image of the first column and amplitude images for other PFM images were almost identical to the presented amplitude images. Adapted from Park *et al.* [21].

3.8 Conclusion

In summary, we demonstrated deterministic mechanical control of multiple domain switching pathways in ferroelectric thin films, rationalized by a concept of trailing flexoelectric field. We selectively produced either purely $r1^-$ or $r3^-$ domains in the BFO thin film by adjusting the motion of a force-loaded but electrically grounded APM tip. We also showed that this mechanical approach has some advantageous features to the conventional electrical approach for deterministic selection of domain switching pathways. Flexoelectric field has much higher magnitude of IP field distribution compared with electrical field which should be crucial for domain selection in low symmetry materials. Also, retention property of the switched domain by mechanical load seems much enhanced. Other than that, there are many advantageous features. Mechanical switching removes the need for a bottom electrode and it also avoids applying a voltage to a thin film, thus, removing the problems of leakage, breakdown and charge injection. Moreover, our work further enhances the idea that mechanical switching is flexoelectric origin rather than adsorbate removal since adsorbates have no bearing on in-plane polarization. Importantly, our work can be a crucial step towards design of memory devices operated by mechanical force since IP polarization can be switched back and forth unlike in OP polarization. Thus, this work opens a new avenue for engineering ferroelectric domains with mechanical force in low-symmetry

materials, particularly by controlling their multiple ferroelectric switching pathways with the nanoscale precision. Finally, this work provides a new insight for constructing novel non-volatile magnetoelectric coupling devices and multilevel data storage.

References

1. Kogan, S. M., *Sov. Phys. Solid State* **5**, 2069 (1964).
2. Catalan, G. *et al.*, *Nat. Mater.* **10**, 963–967 (2011).
3. Lu, H. *et al.*, *Science* **336**, 59–61 (2012).
4. Lee, D., Yang, S. M., Yoon, J. & Noh, T. W., *Nano Lett.* **12**, 6436–6440 (2012).
5. Li, Y.-J. *et al.*, *Adv. Funct. Mater.* **25**, 3405–3413 (2015).
6. Lu, H. *et al.*, *Nano Lett.* **16**, 6460–6466 (2016).
7. Bhaskar, U. K. *et al.*, *Nat. Nanotechnol.* **11**, 263–266 (2015).
8. Narvaez, J., Vasquez-Sancho, F. & Catalan, G., *Nature* **538**, 219–221 (2016).
9. Lee, D. *et al.*, *Phys. Rev. Lett.* **107**, 057602 (2011).
10. Borisevich, A. Y. *et al.*, *Nat. Commun.* **3**, 775 (2012).
11. Jeon, B. C. *et al.*, *Adv. Mater.* **25**, 5643–5649 (2013).
12. Chu, K. *et al.*, *Nat. Nanotechnol.* **10**, 972–979 (2015).
13. Gu, Y., Hong, Z., Britson, J. & Chen, L.-Q., *Appl. Phys. Lett.* **106**, 022904 (2015).
14. Balke, N. *et al.*, *Nat. Nanotechnol.* **4**, 868–875 (2009).
15. Crassous, A., Sluka, T., Tagantsev, A. K. & Setter, N., *Nat. Nanotechnol.* **10**, 614–618 (2015).
16. Vasudevan, R. K. *et al.*, *Nat. Commun.* **5**, 4971 (2014).
17. Matzen, S. *et al.*, *Nat. Commun.* **5**, 4415 (2014).
18. Wang, C. *et al.*, *Nat. Commun.* **7**, 10636 (2016).
19. Baek, S. H. *et al.*, *Nat. Mater.* **9**, 309–314 (2010).

-
20. Jang, B. *et al.*, *Nat. Phys.* **13**, 189–196 (2017).
 21. Park, S. M. *et al.*, *Nat. Nanotechnol.* **13**, 366–370 (2018).
 22. Chu, Y.-H. *et al.*, *Adv. Mater.* **19**, 2662–2666 (2007).
 23. Streiffer, S. K. *et al.*, *J. Appl. Phys.* **83**, 2742–2753 (1998).
 24. Očenášek, J. *et al.*, *Phys. Rev. B* **92**, 035417 (2015).

Chapter 4

Controlling electrical state in dielectrics with mechanical force: colossal flexoresistance

4.1 Introduction

Dielectrics have long been thought to be unsuitable for pure electrical switches[1-3]; under weak electric fields, they show extremely low conductivity, whereas under strong static fields, they suffer from irreversible damage. Recently, applying an ultrashort pulse of strong electric fields has permitted damage-free electrical breakdown and colossal enhancement of conductivity in otherwise insulating dielectrics[4,5]. However, this effect is inevitably transient, so it remains challenging to achieve static, damage-free control of electrical states in dielectrics. To tackle this problem, we thought of another method to apply strong static field; that is flexoelectricity[6-17] of which avoids applying a electric bias thus, possiely removing a problem of breakdown.

Controlling electron dynamics in solids has opened avenues for fascinating physical phenomena[4,5,18] and has formed the basis of electronic applications. In semiconductors with a relatively small but nonzero bandgap, applying moderate electric fields could switch their electrical state, i.e., from insulator to conductor,

which makes them a building block for contemporary digital electronics. In dielectrics with a large bandgap, controlling their electrical states is quite complicated, as it usually involves a combination of intrinsic and extrinsic processes. Zener [1] predicted that strong electric fields ($\geq 10^9$ V m⁻¹) could intrinsically lead to electrical breakdown in dielectrics through tunneling processes across the valence and conduction bands. As this dielectric breakdown naturally guarantees the largest and fastest electrical response, recent works have aimed to realize it by applying strong femtosecond fields [4,5]. Under strong ‘static’ fields, however, the dielectric breakdown has been unavoidably subject to extrinsic effects, such as Joule heating and irreversible damage. This situation complicates our understanding of the intrinsic mechanism of dielectric breakdown and limits device application.

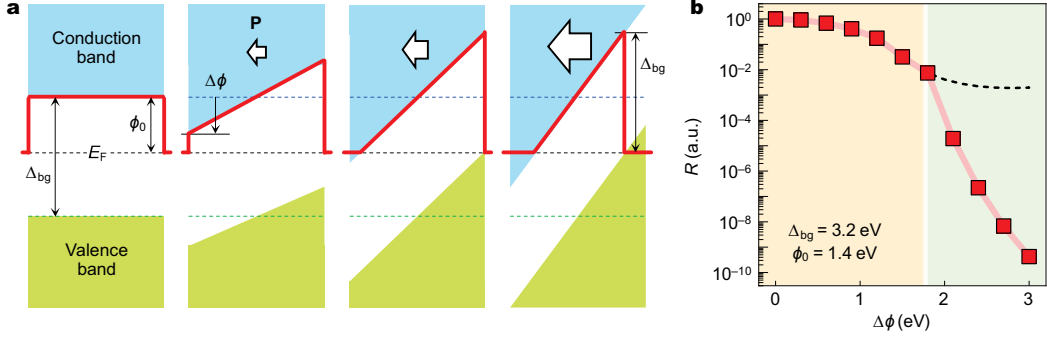


Figure 4.1 Colossal decrease of resistivity in highly polarized ultrathin dielectrics. **a**, Schematic diagram of the potential energy profiles across SrTiO₃ (STO) with increasing flexoelectric polarization (P ; white arrow). Red solid lines and black dashed lines indicate the effective tunnel barrier and Fermi level, respectively. Blue and green dashed lines indicate the conduction band minimum and valence band maximum for $P = 0$, respectively. **b**, Resistance as a function of $\Delta\phi$, obtained by calculating tunneling conductance through a Wentzel–Kramers–Brillouin (WKB) approximation. We normalize the resistance by the value at $\Delta\phi = 0$, and assume the bandgap Δ_{bg} , original barrier height ϕ_0 , and original barrier width d_0 to be 3.2 eV, 1.4 eV, and 3.9 nm, respectively. At $\Delta\phi = 1.8$ eV, the valence band maximum crosses the Fermi level, which causes an abrupt reduction in the resistance. The black dashed line indicates the result obtained by neglecting the valence band contribution. Adapted from Park *et al.* [31].

To achieve intrinsic, static control of electrical states in dielectrics, we could utilize a non-destructive electrostatic field developed in ultrathin polar materials (Fig. 4.1a). When a polar material is sufficiently thin but still maintains polarization P , a depolarization field E_{dep} arises from the unscreened bound charges on its surface [19,20]:

$$E_{dep} = -\frac{P - \sigma_s}{\epsilon} \quad (4.1)$$

where σ_s is the screening charge (e.g., by adjacent metal electrodes) and ϵ is the

dielectric permittivity of the polar material. In the ultrathin limit, σ_S tends to zero [20] and E_{dep} becomes increasingly saturated at $E_{\text{dep}} = -P/\epsilon$, largely modifying the band structure (Fig. 1a). In particular, when the polarization exceeds a certain threshold, both the conduction band minimum and valence band maximum could cross the Fermi level, as confirmed in our first-principles calculation (Fig. 4.2). In such a case, the tunnel barrier width of ultrathin dielectrics would abruptly decrease, whereas the tunnel barrier height remains fixed to the bandgap Δ_{bg} (Fig. 4.1a and Fig. 4.3). This would result in a significant enhancement of tunneling conductance across ultrathin dielectrics, leading to a colossal decrease in electrical resistance, as predicted in our Wentzel–Kramers–Brillouin (WKB) simulation (Fig. 4.1b, see appendix C for detailed method). Therefore, it would be of great interest to explore tunnel transport across a highly polarized ultrathin dielectric.

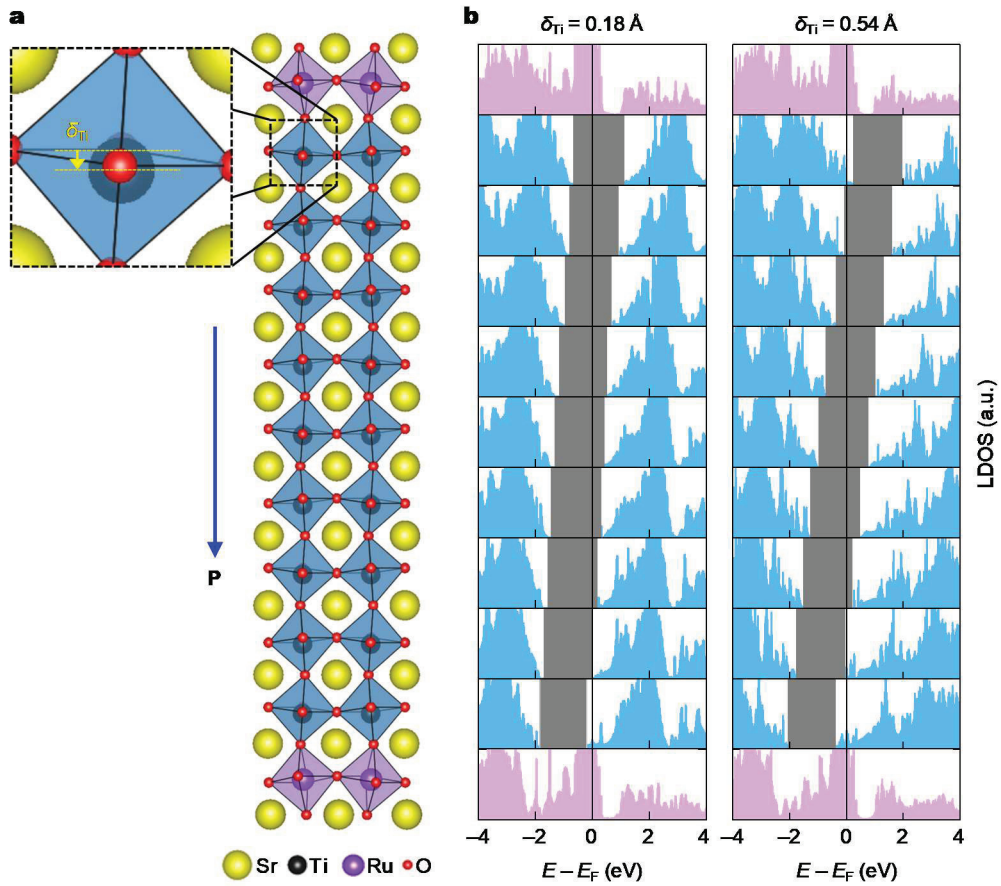


Figure 4.2 Polarization-induced band crossing of STO conduction and valence bands. **a**, The simulation cell. We artificially polarized STO layers with uniform displacement of a Ti atom by δ_{Ti} . **b**, Calculated layer-resolved density of states (LDOS; filled blue) of polarized STO layers with $\delta_{\text{Ti}} = 0.18 \text{ \AA}$ (left) and 0.54 \AA (right). Gray regions represent a gap between the conduction band minimum and valence band maximum of polarized STO layers, clearly showing a shift in the energy bands due to a polarization-induced electric field. Adapted from Park *et al.* [31].

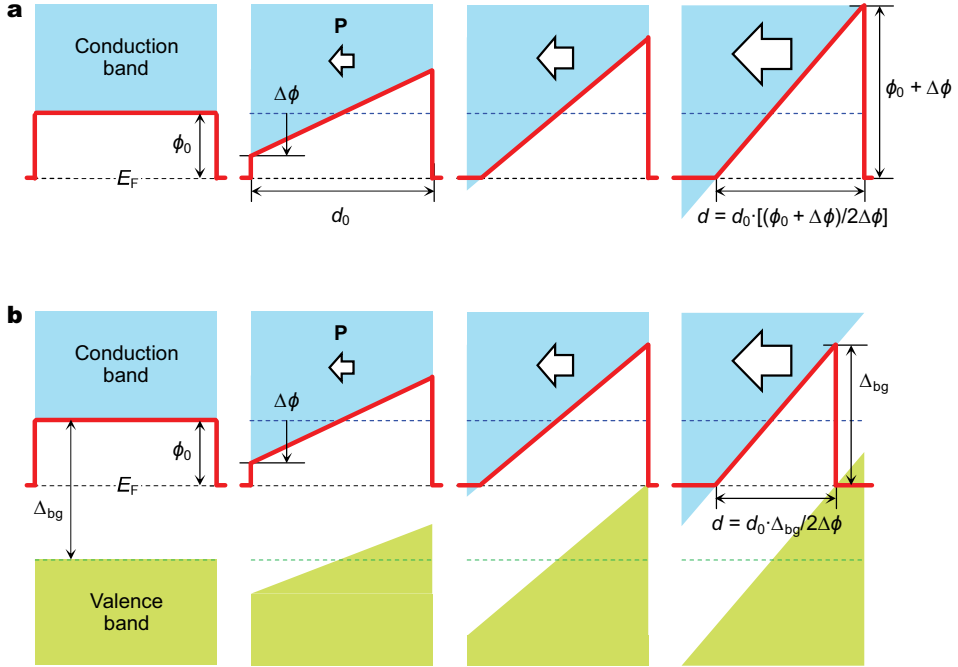


Figure 4.3 Schematic diagram of the potential energy profiles across polarized STO. a,b, Red solid lines indicate the effective tunnel barrier with increasing flexoelectric polarization (P ; white arrow) with (a) and without (b) considering the contribution of the STO valence band. Black dashed lines indicate the Fermi level. Blue and green dashed lines indicate the conduction band minimum and valence band maximum for $P = 0$, respectively. Adapted from Park *et al.* [31].

To this end, we can induce and stabilize large polarization in an ultrathin dielectric via flexoelectricity [6-15]. All dielectric materials polarize in response to strain gradients, as follows:

$$P = \varepsilon \cdot f_{\text{eff}} \cdot \frac{\partial u}{\partial x} \quad (4.2)$$

where $\partial u / \partial x$ and f_{eff} are the strain gradient and effective flexocoupling coefficient, respectively. Applying loading forces through an atomic force microscope (AFM)

tip generates strain gradients as large as 10^7 m^{-1} in ultrathin dielectrics [10,16]. Such giant strain gradient could then induce flexoelectric polarization, up to a few 0.1 C m^{-2} (ref. [16]), much larger than the polarization values typically attainable in ultrathin ferroelectrics [21,22]. In this chapter, I will show that flexoelectricity [6-17] enables damage-free exposure of dielectrics to strong static fields, leading to colossal control of conductivity. Applying strain gradients with an atomic force microscope tip polarizes an ultrathin film of an archetypal dielectric SrTiO_3 (STO) via flexoelectricity [10,16], which in turn generates non-destructive, strong electrostatic fields. When the applied strain gradient exceeds a certain value, STO suddenly becomes highly conductive, yielding at least around 10^8 -fold decrease in room-temperature resistivity. We explain this phenomenon, which we call “colossal flexoresistance”, based on the abrupt increase in the tunneling conductance of ultrathin STO under giant strain gradients.

4.2 Estimation of threshold polarization above which both the conduction band minimum and valence band maximum cross the Fermi level

We used contact mechanics analysis to simulate strain gradients and associated flexoelectric polarization in ultrathin STO under an AFM tip loading force (see appendix D for detailed procedure). For the simulation, we adopt a diamond tip and assume a tip radius of curvature (r_{tip}) of 150 nm. Figure 4.4a shows a simulated profile of transverse strain u_{11} under a representative tip loading force

of 15 μN , revealing the large inhomogeneity of u_{11} . The resulting transverse strain gradients $\partial u_i/\partial x_3$ (i.e., $= \partial u_{11}/\partial x_3 + \partial u_{22}/\partial x_3$) are as huge as a few 10^7 m^{-1} (Fig. 4.5); this giant strain gradients are attributable to AFM tip-induced downward bending at the nanoscale. Our simulation also finds that those strain gradients induce large polarization in ultrathin STO via flexoelectricity, reaching up to 0.19 C m^{-2} on average (Fig. 4.4b). When neglecting flexoelectricity, our simulation does not produce any polarization, confirming the flexoelectric nature of the induced polarization (not shown here).

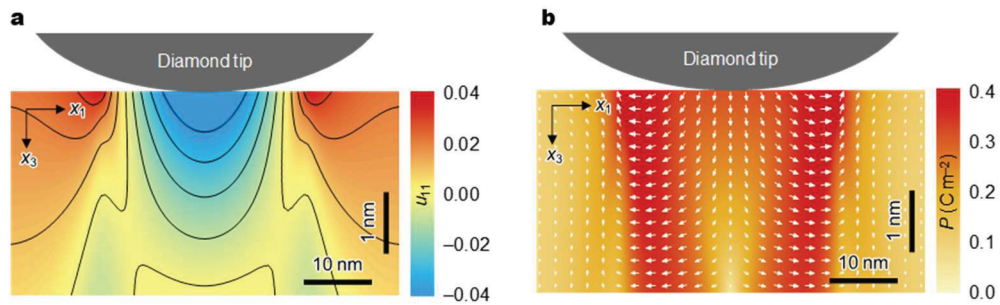


Figure 4.4 Mechanically induced large polarization in ultrathin dielectrics. a,b, Phase-field simulations for the transverse strain u_{11} (a) and corresponding polarization distribution (b) in 10 unit cell-thick (i.e., 3.9 nm-thick) STO under a representative tip loading force of 15 μN over a circular area $\sim 13 \text{ nm}$ in radius. Adapted from Park *et al.* [31].

When such a large polarization remains preserved in an ultrathin dielectric, it could significantly modify the band structure of the dielectric, as predicted in Fig. 4.1. We estimate the threshold polarization P_{th} in ultrathin STO, above which both the conduction band minimum and valence band maximum cross the Fermi level (Fig. 4.1a):

$$|P_{\text{th}}| \approx \varepsilon \cdot E_{\text{dep,th}} = \varepsilon \cdot \frac{\Delta_{\text{bg}}}{e \cdot t} \quad (4.3)$$

where Δ_{bg} and t are the bandgap and thickness of the STO layer, respectively, e is the electronic charge, and $E_{\text{dep,th}}$ is the threshold E_{dep} . Given that $\varepsilon \sim 20\varepsilon_0$ of strained STO (Fig. 4.6), $\Delta_{\text{bg}} = 3.2$ eV and $t = 3.9$ nm, equation (3) yields $P_{\text{th}} = 0.15$ C m⁻², comparable to the value obtained in our simulation (Fig. 4.4b). At a certain AFM-tip loading force, therefore, the induced flexoelectric polarization could give rise to an abrupt increase in tunneling currents across ultrathin STO.

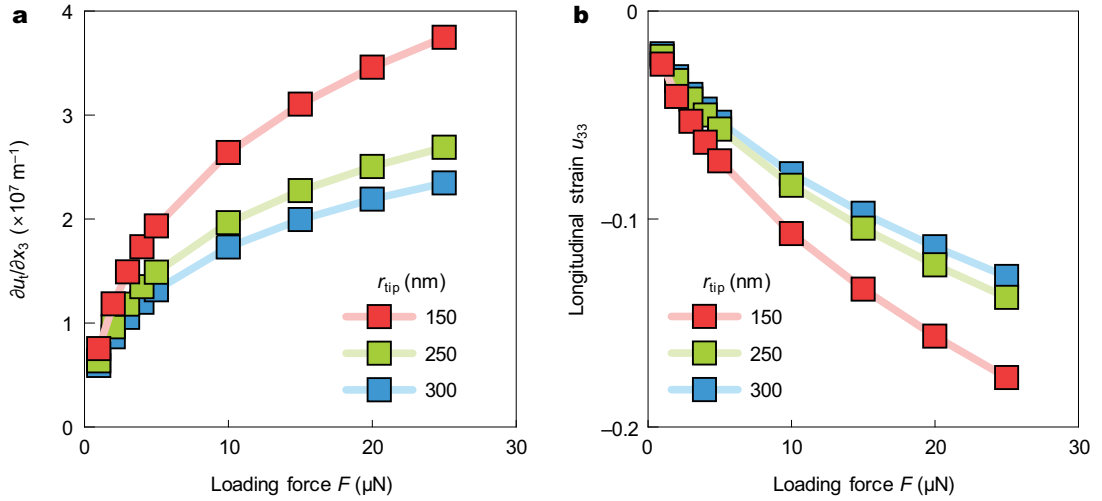


Figure 4.5 Calculated strain gradients and strains imposed by the AFM tip. **a**, The averaged transverse strain gradients $\partial u_i / \partial x_3$ under the tip as a function of loading force. **b**, The averaged longitudinal strains u_{33} under the tip as a function of loading force. Adapted from Park *et al.* [31].

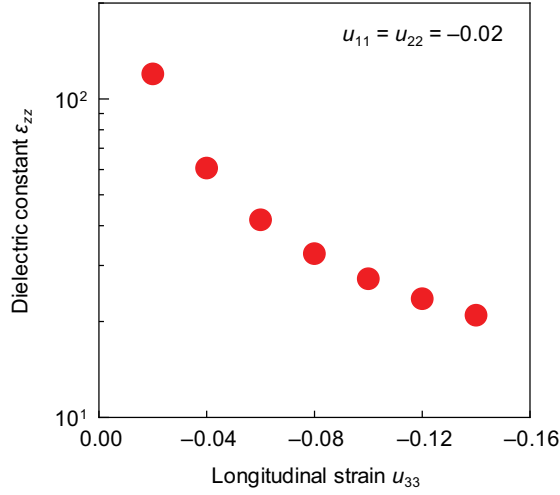


Figure. 4.6. Calculated dielectric constants. Density functional theory (DFT) calculations on the total zz component of the total dielectric constant (i.e., ϵ_{zz}), which includes both ionic and electronic contributions, as a function of longitudinal strain u_{33} . We fixed the transverse strains u_{11} and u_{22} to -0.02 . The strain was measured with respect to the DFT equilibrium lattice of 3.86 \AA . Adapted from Park *et al.* [31].

4.3 Experimental results and discussion

4.2.1 Sample preparation

We choose SrTiO_3 (STO) as a model dielectric system, as it shows enhanced flexocoupling strength at the nanoscale [16], as well as a reasonably large bandgap of 3.2 eV. Importantly, furthermore, its conductivity responds negligibly to the applied strain itself (Fig. 4.7) [23,24], thereby maximizing the contribution from strain gradient-induced flexoelectricity. We prepare 10 unit cell-thick (i.e., 3.9 nm-thick) stoichiometric STO films on a (001)-oriented STO single crystal substrate, with a conductive SrRuO_3 buffer layer (Fig. 4.8). SrRuO_3 and STO thin

films

were

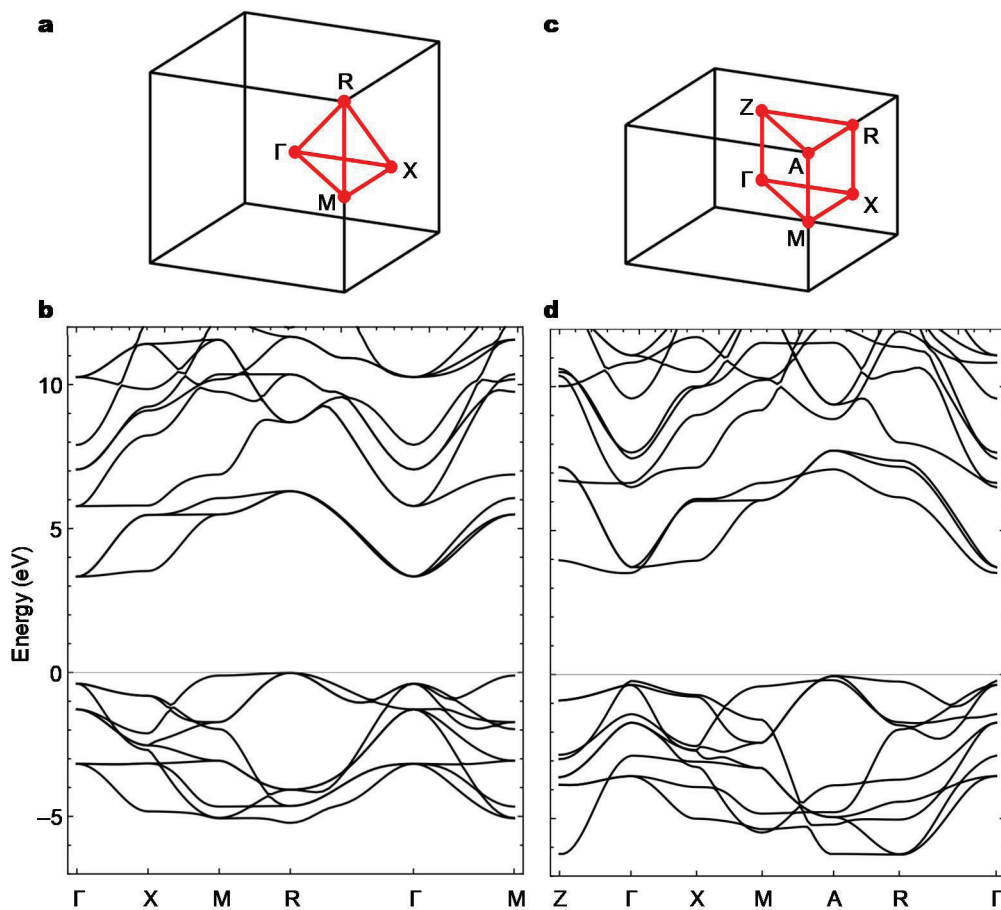


Figure 4.7 Negligible strain effect in the STO bandgap. a,b, The Brillouin zone of a simple cubic STO ($a = 3.897 \text{ \AA}$) with the special k points (a) and corresponding band structure (b). c,d, The Brillouin zone of a strained tetragonal STO ($a = 3.819 \text{ \AA}$, $c = 3.508 \text{ \AA}$) with the special k points (c) and corresponding band structure (d). The zero of energy is set at the valence-band maximum. Adapted from Park *et al.* [31].

sequentially grown on TiO_2 -terminated and (100)-oriented STO substrates. The growth dynamics and thickness were monitored by in-situ reflection high-energy electron diffraction (RHEED; Fig. 4.8). Film deposition was performed at 700°C under oxygen partial pressure of 100 and 7 mTorr for SrRuO_3 and STO, respectively.

After deposition, films were annealed at 475°C for 1 h in oxygen at ambient pressure and subsequently cooled to room temperature at 50°C min⁻¹. Structural characterization, namely, reciprocal space mapping was performed to ensure that the STO film was strain-free. The stoichiometric homoepitaxial STO should remain paraelectric down to 0 K (ref. [25]); however, under an AFM tip loading force, it can become highly polarized via flexoelectricity [16].

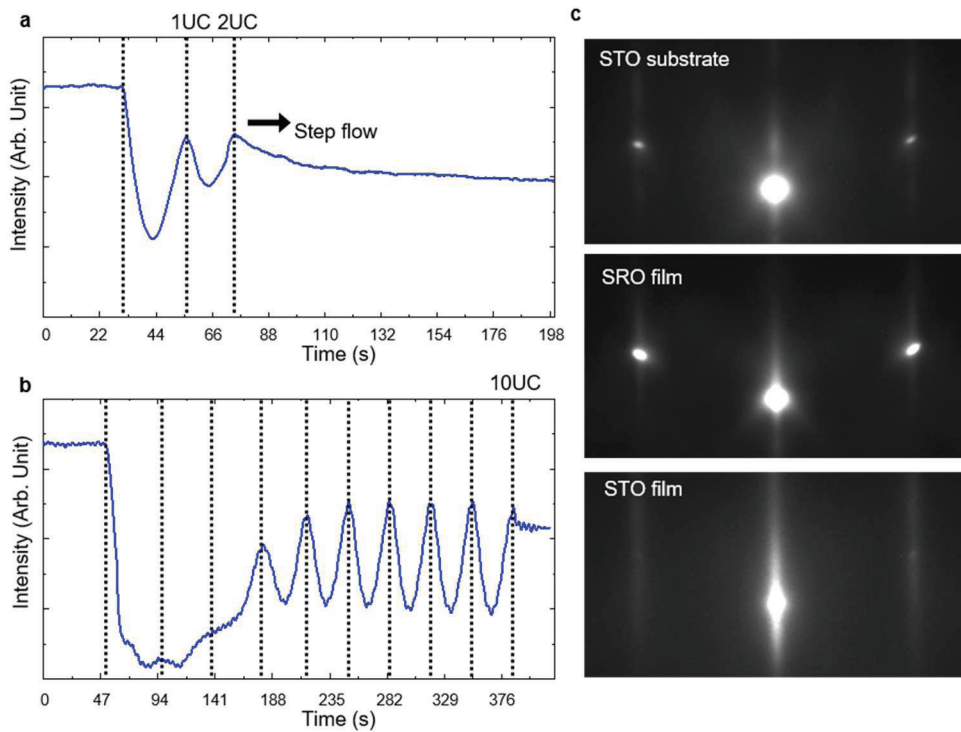


Figure 4.8 Growth and characterization of ultrathin homoepitaxial STO. **a,b** Reflection high energy electron diffraction (RHEED) oscillations obtained during the growth procedure of (a) SrRuO₃ and (b) STO films via pulsed laser deposition method, indicating the growth mode and the thickness of the films. **c**, *In-situ* reflection high energy electron diffraction of STO substrate, SrRuO₃ film and STO film. Adapted from Park *et al.* [31].

4.2.2 Local I–V measurement with various applied forces with AFM tip on 10 u.c. STO ultrathin film

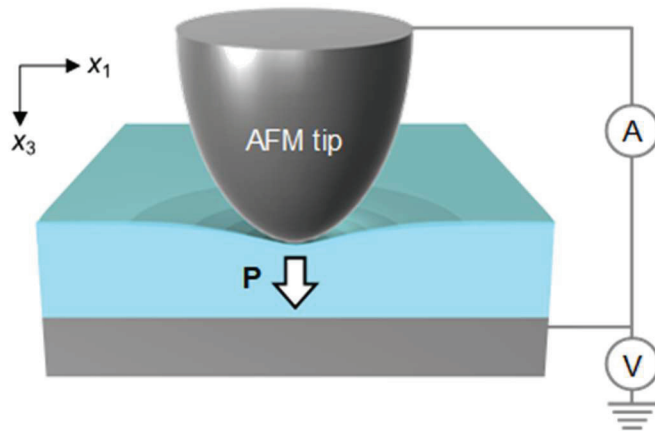


Figure 4.9 Local I–V measurement setup with mechanical gating with AFM tip. Schematic diagram of the experimental setup, illustrating the flexoelectric polarization (white arrow) generated by the atomic force microscope (AFM) tip pressing the surface of ultrathin dielectrics. While generating large strain gradients, we simultaneously measure the tunneling currents across the flexoelectrically polarized STO. Adapted from Park *et al.* [31].

We use a conductive AFM tip to apply loading forces while simultaneously measuring the tunneling current (Fig. 4.9). Conforming to the simulation condition, we use a diamond-coated tip with $r_{\text{tip}} = 150$ nm, which also can withstand much higher loading forces than other conductive tips (e.g., PtIr-coated tips). The detailed experimental conditions are as follow: The I – V curves were obtained using an Asylum Research Cypher AFM (Oxford Instruments, Abingdon, UK) at room temperature under ambient conditions. Conducting diamond-coated metallic tips (DDESP-V2; BRUKER, Billerica, MA, USA) with nominal spring constants 80 N m^{-1} and a dual-gain ORCA module (Oxford

Instruments) were used to measure currents. An electrical bias was applied through the conducting SrRuO₃ electrode; this was swiped from -0.5 V to $+0.5$ V at a ramping rate of about 4 V s⁻¹. During the measurements, we set the current limit (compliance) to 20 nA. The noise floor of the AFM system was about \sim few pA.

Figure 4.10 shows the current–voltage (I – V) curves measured at room temperature for a few representative loading forces. At small applied forces (up to 7 μ N), the measured current remains close to the noise level (~ 1 pA). At intermediate applied forces (ranging from 7 to 13 μ N), the I – V curves exhibit typical tunneling characteristics, and the current level increases gradually with the applied force. These results are ascribable to systematic modification of tunnel-barrier profiles under AFM tip loading forces, consistent with our previous work [16]. Interestingly, when the applied forces exceed a threshold value (~ 15 μ N), the I – V curves suddenly become linear in shape—characteristic of a highly conducting state. This highlights that the electrical state of ultrathin STO is switchable between highly insulating and conducting states, via purely mechanical means.

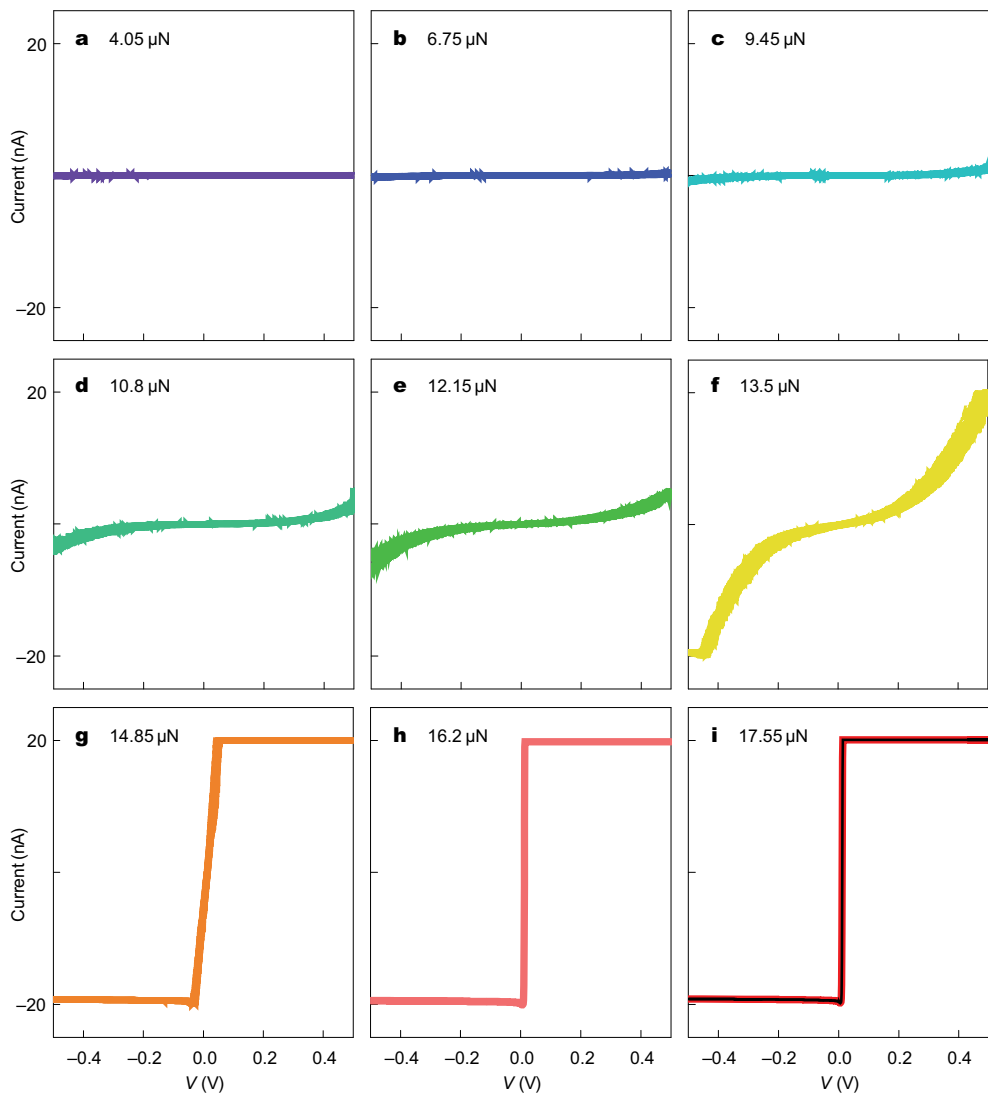


Figure 4.10 Tunneling currents across a 10 unit cell-thick STO film. a–i, Tunneling currents with increasing forces. Before the critical force, I – V curves show tunneling like behavior and the magnitude increases gradually as the applied force increases. After the critical force, I – V curves show linear-like behavior. During the measurements, we set the current limit (compliance) to 20 nA. A black solid line in i indicates the I – V curve measured for a bare SrRuO₃ thin film, based on which we estimate the resistance of the bottom SrRuO₃ layer to be ~ 70.4 k Ω . Adapted from Park *et al.* [31].

4.2.3 Colossal flexoresistance in ultrathin STO film

Importantly, this electrical state switching in a large-bandgap dielectric naturally leads to an extremely large change in the electrical resistivity. We measured the resistance R from the linear slope of I - V curves (Fig. 4.10) in the low-bias regime. We extracted the resistance of STO, i.e., R_{STO} , from the difference between the measured R and the resistance of the bottom SrRuO₃ layer (i.e., ~ 70.4 k Ω ; Fig. 4.10i). We then estimated an effective resistivity (ρ_{eff}) of STO by considering the effective tip-STO contact radius (a) and the effective STO thickness (t_{STO}):

$$\rho_{\text{eff}} = R_{\text{STO}} \cdot \frac{\pi a^2}{t_{\text{STO}}} \quad (4.4)$$

where we obtained the values of a and t_{STO} from our theoretical contact mechanics analysis (Fig. 4.5). During electrical state switching, the effective resistivity of STO exhibits a colossal change with around eight orders of magnitude difference for the case of tip with 150nm r_{tip} (Fig. 4.11b). Due to the detection limit of our equipment, we may underestimate the resistivity of the insulating state, i.e., 10^7 Ω cm, compared to the bulk STO resistivity of over 10^9 Ω cm; thus, the actual

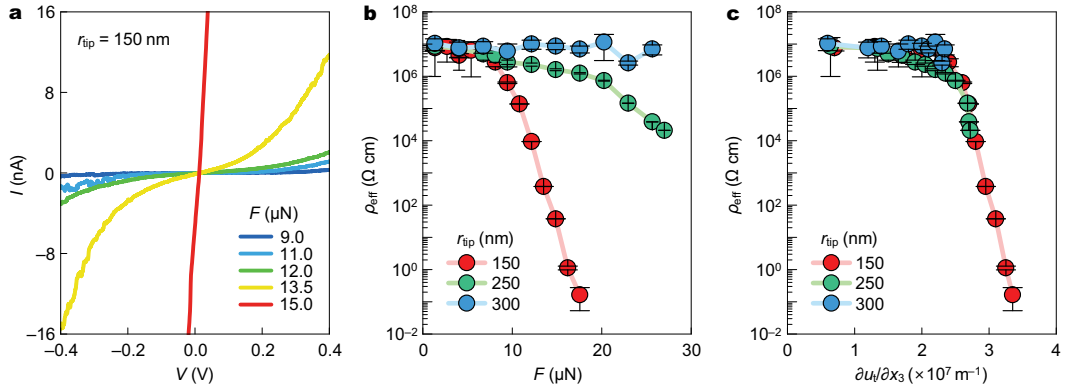


Figure 4.11 Colossal flexoresistance effect in ultrathin STO. **a**, Current–voltage (I – V) curves obtained by conductive AFM measurements in a 10 unit cell-thick STO film upon application of various tip loading forces F . Five representative curves are shown here. **b**, Effective resistivity (ρ_{eff}) as a function of F . **c**, ρ_{eff} as a function of the AFM tip-induced strain gradient $\partial u/\partial x_3$. Adapted from Park *et al.* [31].

ratio of resistivity change could be larger than the estimated value. Given that we estimate the effective resistivity by taking into account the loading force dependence of the tip–STO contact area and STO thickness, we exclude any geometric anomaly as an origin for the observed effect. When we normalize the measured effect by applied pressures (i.e., loading forces divided by the tip–STO contact area), the relative increase in conductivity turns out to be as large as 10^{-2} Pa^{-1} (Fig. 4.12). Compared to other pressure-induced effects, such as piezoresistance (at most, 10^{-7} Pa^{-1}) [26,27], this effect not only shows orders-of-magnitude enhancement, but also implies a distinctly new mechanism.

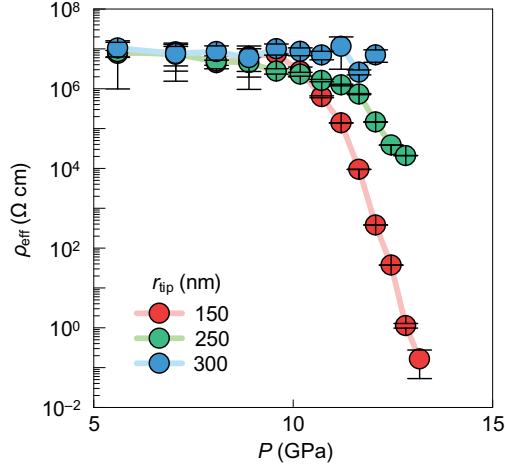


Figure 4.12 Pressure dependence of the resistivity. Although the tips with $r_{\text{tip}} = 250$ and 300 nm can generate pressure, comparable to that by the tip with $r_{\text{tip}} = 150$ nm, the resulting resistivity changes are suppressed considerably. Adapted from Park *et al.* [31].

Furthermore, we also repeat the experiments using AFM tips with different r_{tip} values of ~ 250 and ~ 300 nm (Fig. 4.13). In order to estimate the tip radius (r_{tip}) from the measured SEM images, we digitized the profile of the tip shape using a Java-based software (plot digitizer 2.6.8). The outline of the tip was tracked down with a scale of a pixel (~ 35 nm) in SEM images. Digitized data points were fitted with parabolic function, then converted into r_{tip} as follows.

$$y(x) = ax^2 + bx + c \quad (4.5)$$

$$r_{\text{tip}} = \left[\frac{1}{|2(a-\sigma_a)|} + \frac{1}{|2(a+\sigma_a)|} \right] / 2, \quad (4.6)$$

where σ_a is the standard error of a .

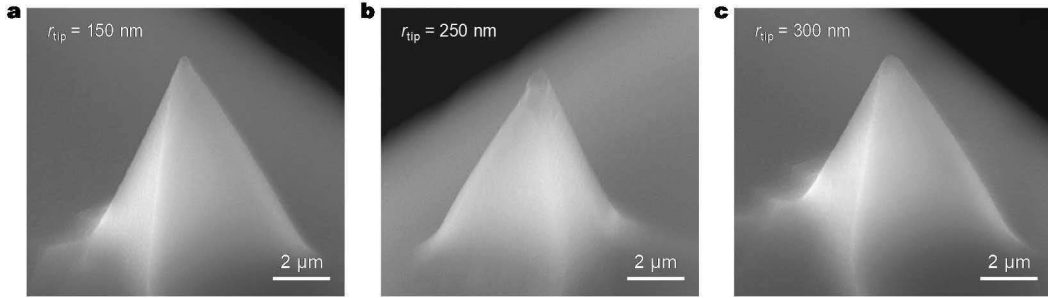


Figure 4.13 Microscopic images of AFM tips. a–c, Scanning electron microscopy images of diamond-coated AFM tips with an r_{tip} estimated to be around 150 nm (a), 250 nm (b) and 300 nm (c). Adapted from Park *et al.* [31].

The experiments using AFM tips with different r_{tip} values of ~ 250 and ~ 300 nm show quite different behavior (Figure. 4.11c,d and Fig. 4.12). Although these tips can generate longitudinal strain u_{33} , comparable to that by the tip with $r_{\text{tip}} = 150$ nm (Fig. 4.5), the resulting resistivity changes are suppressed considerably (Fig. 4.11b). Therefore, these results suggest that the observed colossal decrease in resistivity could originate from AFM tip-induced strain gradients, which modify the tunnel barrier via flexoelectricity.

Figure 4.11c indeed highlights the close correlation between the resistivity change and strain gradients. Strikingly, all of the data obtained with the three tips collapse to a nearly single curve when plotting the resistivity as a function of $\partial u_l / \partial x_3$. This emphasizes the dominant contribution of $\partial u_l / \partial x_3$ to the observed colossal reduction of resistivity. As predicted in Fig. 4.1, when the strain gradient-induced flexoelectric polarization reaches a threshold value, both the conduction band minimum and valence band maximum cross the Fermi level. This band crossing is capable of not only enhancing the tunneling conductance across STO (Fig. 4.1b)

but also promoting interband tunneling between the STO valence and conduction bands, causing Zener breakdown[1,18,28]. Equations (4.2) and (4.3) estimate the threshold $\partial u/\partial x_3$ required for the band crossing to be around $3 \times 10^7 \text{ m}^{-1}$ for 10 unit cell-thick STO, using $\Delta_{\text{bg}} = 3.2 \text{ eV}$, $t = 3.9 \text{ nm}$, and $f_{\text{eff}} = 25 \text{ V}$ (ref. ¹⁶). This agrees quantitatively with our experimental results (Fig. 3c), in which the colossal decrease of resistivity begins at $\partial u/\partial x_3 \sim 2.5 \times 10^7 \text{ m}^{-1}$. Taken together, our experimental and theoretical results consistently evidence that flexoelectric polarization-induced band crossing could explain the colossal reduction of resistivity, which we call the “colossal flexoresistance”.

4.2.4 Local I–V measurement with various applied forces with AFM tip on 10 u.c. BaTiO₃ and LaAlO₃ ultrathin film

As such, it would be interesting to explore colossal flexoresistance in other dielectrics. As flexoelectricity is a universal phenomenon in all dielectrics, colossal flexoresistance could, in principle, be universal as well. Each dielectric, however, would require different threshold loading forces (i.e., threshold strain gradients) for colossal flexoresistance, depending on the inherent flexocoupling strength, bandgap, and so on. We repeat the experiments using BaTiO₃ and LaAlO₃ of similar thicknesses (i.e., 10 unit cell-thick). For BaTiO₃, we observe the same electrical-state switching (Fig. 4.14a), but at a lower threshold loading force. The lower threshold loading force may originate from inherently larger flexocoupling strength in BaTiO₃ (ref. [29]), compared to that in STO. For

LaAlO₃, contrarily, we do not observe any noticeable resistance change up to the maximum AFM-tip loading force (Fig. 4b). LaAlO₃ may have a much weaker flexocoupling strength due to its small Born effective charge [30]; additionally, its large bandgap (i.e., $\Delta_{\text{bg}} = 5.5$ eV) also requires a large threshold polarization in equation (4.2). These conditions may make the threshold strain gradient in LaAlO₃ too large to be achievable in our experimental geometry.

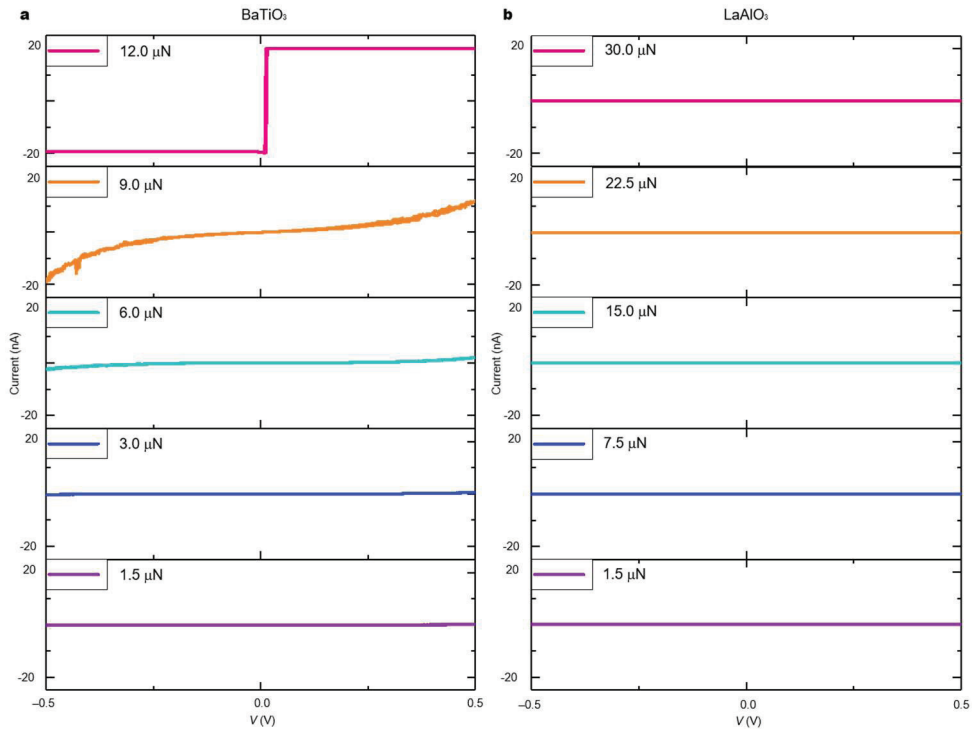


Figure 4.14 Local I - V measurements with different dielectric materials such as BaTiO₃ and LaAlO₃. a,b, Tunneling currents across a 10 unit cell-thick BaTiO₃ (a) and LaAlO₃ (b) film. Adapted from Park *et al.* [31].

4.2.5 Local I - V measurement with various applied forces with AFM tip on

Graphene/10 u.c. BaTiO₃ ultrathin film

We also reproduce the same result even using a graphene top electrode (Fig. 4.15). This again excludes any electrochemical interaction of STO with experimental environments, such as the AFM tip or ambient atmosphere, as graphene is impermeable to all atoms and molecules. For the graphene transfer onto the ultrathin BaTiO₃ film, the so-called dry-transfer technique was used. A graphene monolayer was mechanically exfoliated on a silicon wafer coated with poly(vinyl alcohol) (PVA), which is water-soluble, and poly(methyl methacrylate) (PMMA). After the selection of a proper graphene flake, the flake/ PMMA layer was detached from the silicon substrate by immersion in hot deionized water. After that, the flake/PMMA layer floating on the water was transferred to a holder and was placed on the ultrathin BaTiO₃ film using a homemade micromanipulator after alignment under an optical microscope. At last, the PMMA was removed with acetone.

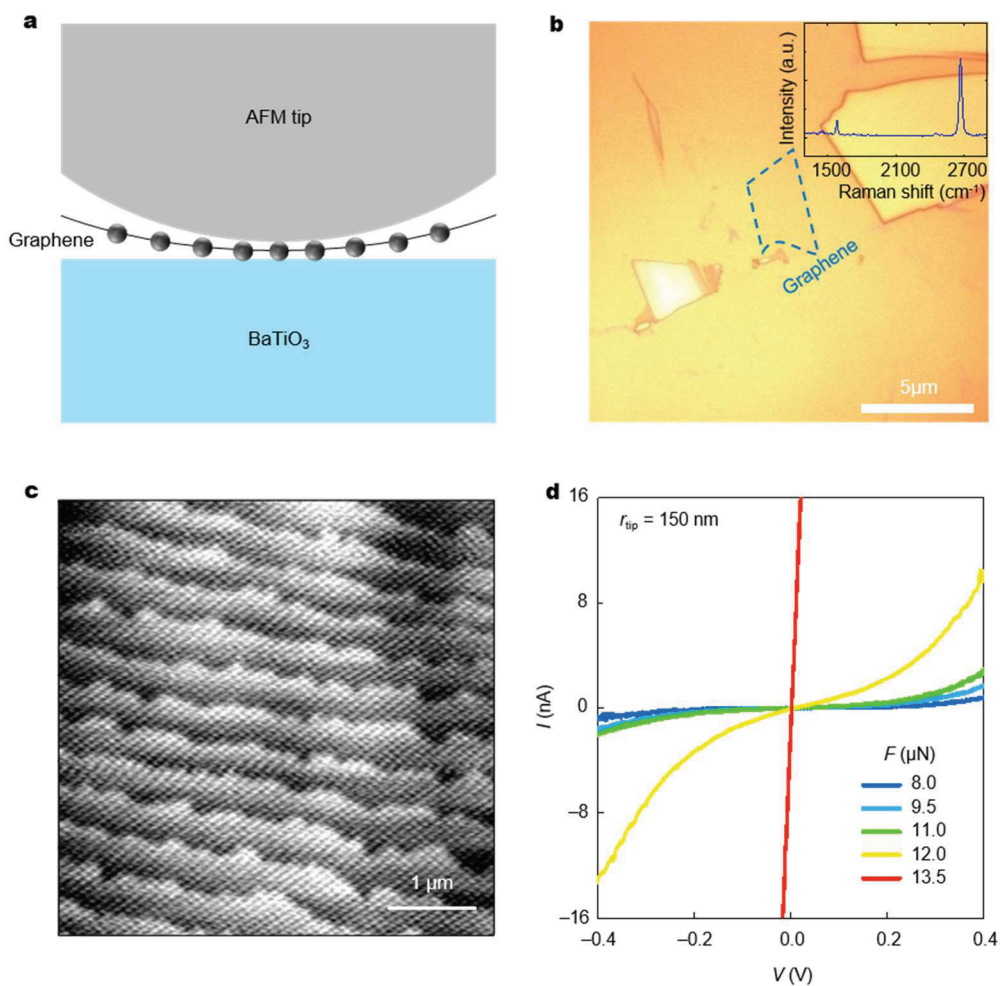


Figure 4.15 Colossal flexoresistance in a 10 unit cell-thick BaTiO₃ film, buffered with a graphene. **a**, A schematic of experimental geometry with the graphene-buffered BaTiO₃ (Gr/BTO) film. **b**, An optical microscopy image of the Gr/BTO sample surface. Inset corresponds to Raman spectrum of an exfoliated graphene indicating monolayer. **c**, An atomic force microscopy image of the Gr/BTO sample surface. **d**, Tunneling currents across the Gr/BTO sample with increasing tip loading forces. Adapted from Park *et al.* [31].

4.2.6 Reversible operation and on-off state realized by mechanical force

Additional experiments elaborate that this colossal resistance change is reversible, ruling out a possible crack-induced phenomena or electrochemical process as the origin of this transition (Fig. 4.16). The AFM tip-induced mechanical force does not cause any permanent surface damage to the STO film as can be deduced from the surface topography and C-AFM mapping after the several measurements on various regions (Figs. 4.16a,b). Also, the colossal control of resistance is reproducible, as proven by repeated exertion/withdrawal of the loading force (Fig. 4.16c). We sequentially apply both the low ($2 \mu\text{N}$) force and the high force ($15 \mu\text{N}$) in 10 u.c. STO film. Interestingly, on-and-off states can be stably obtained, indicating that no extrinsic damage occurs in the system. Also, this reversibility is valid for 10 u.c. BaTiO_3 as well. These experimental observations suggest that the colossal conductivity change is an intrinsic effect that possibly stems from the flexoelectric polarization-induced modification of the band structure of the dielectrics.

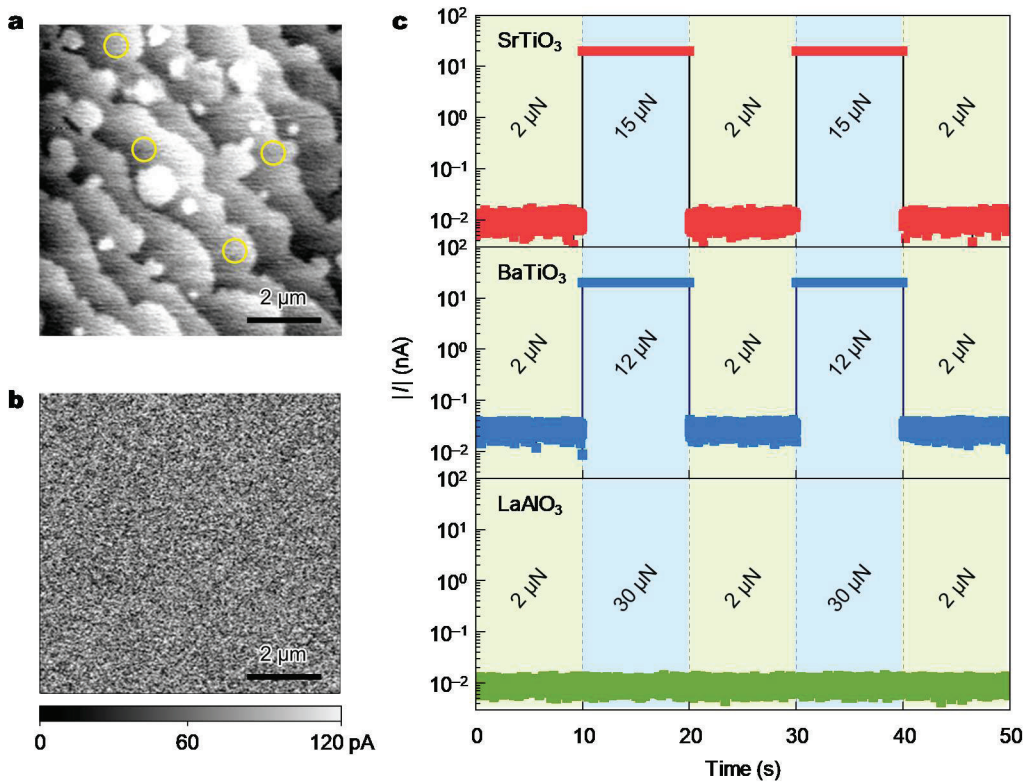


Figure 4.16 Reversible flexoresistance effect. **a**, Topographical image obtained after the experiment. Regions where the experiments were conducted are marked by yellow circles. **b**, Current mapping image with a 1-V bias voltage on the same area, indicating that no current hotspot has been made after the experiment. **c**, Current measured with a 0.1-V bias voltage under two representative loading forces in STO (red symbols), BaTiO₃ (blue symbols) and LaAlO₃ (green symbols). During the measurements, we set the current limit (compliance) to 20 nA. Adapted from Park *et al.* [31].

4.4 Conclusion

The colossal flexoresistance effect described here overcomes a long-standing dilemma: the electrical-state switching in dielectrics requires strong fields, but when applied by strong static fields, dielectrics inevitably suffer from irreversible damage. Utilizing universal flexoelectricity, we develop a general approach to apply non-destructive, strong electrostatic fields in various insulating systems, such as the Mott insulator [18]. Our approach will open up new avenues for unconventional quantum phenomena under strong static fields and device applications, such as the flexoelectronic transistor and mechanical sensor.

References

- [1] Zener, C., *Proc. R. Soc. Lond. A* **145**, 523-529 (1934).
- [2] Jones, S. C., Braunlich, P., Casper, R. T., Shen, X. A. & Kelly, P., *Opt. Eng.* **28**, 1039–1068 (1989).
- [3] Lenzner, M. *et al.*, *Phys. Rev. Lett.* **80**, 4076-4079 (1998).
- [4] Schiffrin, A. *et al.*, *Nature* **493**, 70-74 (2013).
- [5] Schultze, M. *et al.*, *Nature* **493**, 75-78 (2013).
- [6] Tagantsev, A. K., *Phys. Rev. B* **34**, 5883–5889 (1986).
- [7] Zubko, P., Catalan, G., Buckley, A., Welche, P. R. L. & Scott, J. F., *Phys. Rev. Lett.* **99**, 167601 (2007).
- [8] Lee, D. *et al.*, *Phys. Rev. Lett.* **107**, 057602 (2011).
- [9] Catalan, G. *et al.*, *Nat. Mater.* **10**, 963-967 (2011).
- [10] Lu, H. *et al.*, *Science* **336**, 59-61 (2012).
- [11] Chu, K. *et al.*, *Nat. Nanotechnol.* **10**, 972-979, (2015).
- [12] Bhaskar, U. K. *et al.*, *Nat. Nanotechnol.* **11**, 263-266 (2016).
- [13] Narvaez, J., Vasquez-Sancho, F. & Catalan, G., *Nature* **538**, 219-221 (2016).
- [14] Park, S. M. *et al.*, **13**, 366-370 (2018).
- [15] Yang, M. M., Kim, D. J. & Alexe, M., *Science* **360**, 904-907 (2018).
- [16] Das, S. *et al.*, *Nat. Commun.* **10**, 1-7 (2019).

-
- [17] Wang, B., Gu, Y., Zhang, S. & Chen, L.-Q., *Progress in Materials Science* (in press).
- [18] Yamakawa, H. *et al.*, *Nat. Mater.* **16**, 1100-1105 (2017).
- [19] Velev, J. P., Burton, J. D., Zhuravlev, M. Y. & Tsymbal, E. Y., *Npj Comput. Mater.* **2**, 16009 (2016).
- [20] Zhuravlev, M. Y., Sabirianov, R. F., Jaswal, S. S. & Tsymbal, E. Y., *Phys. Rev. Lett.* **94**, 246802 (2005).
- [21] Junquera, J. & Ghosez, P., *Nature* **422**, 506-509 (2003).
- [22] Lu, H. *et al.*, *Adv. Mater.* **24**, 1209-1216 (2012).
- [23] Khaber, L., Beniaiche, A. & Hachemi, A., *Solid State Commun.* **189**, 32-37 (2014).
- [24] Dai, L. D. *et al.*, *J. Phys.-Condens. Matter* **28**, 475501 (2016).
- [25] Lee, D. *et al.*, *Science* **349**, 1314-1317 (2015).
- [26] He, R. R. & Yang, P. D., *Nat. Nanotechnol.* **1**, 42-46 (2006).
- [27] Domingo, N. *et al.*, *Nanoscale* **7**, 3453-3459 (2015).
- [28] Singh-Bhalla, G. *et al.*, *Nat Phys* **7**, 80-86 (2011).
- [29] Narvaez, J., Saremi, S., Hong, J. W., Stengel, M. & Catalan, G., *Phys Rev Lett* **115**, 037601 (2015).
- [30] Behtash, M., Nazir, S., Wang, Y. Q. & Yang, K. S., *Phys. Chem. Chem. Phys.* **18**, 6831-6838 (2016).

[31] S. M. Park *et al.* Colossal flexoresistance in dielectrics, Submitted.

Chapter 5

Conclusion

Over the last decade, flexoelectric effect at nanoscale in solid has shown their wide potential both scientifically and technologically. There are already some patents for commercial electronic devices to replace piezoelectric devices such as sensor, and actuator. Also, they have shown rich and intriguing physical phenomena, including the recent hot topic of domain wall and photovoltaic. Despite these extensive studies on flexoelectric effect, I believe that many interesting issues still remain untouched. In this thesis, two novel findings have been addressed: trailing flexoelectric field for manipulation of multiaxial ferroelectric, control of electrical state in dielectric with flexoelectric origin.

Firstly, I have demonstrated that in multiaxial ferroelectric epitaxial films, the trailing flexoelectric field generated by mobile AFM tip pressing can be used as an effective tool for engineering domain structures. We have suggested several advantageous features over electrical way. Also, we have overcome serious drawback of mechanical switching of ferroelectric polarization with AFM tip that is switching is unidirectional, i.e. only switching of polarization up to down is possible. I believe that the finding of this mechanism of trailing flexoelectric will open a great possibility to study exotic ferroelectric domain by creating it without

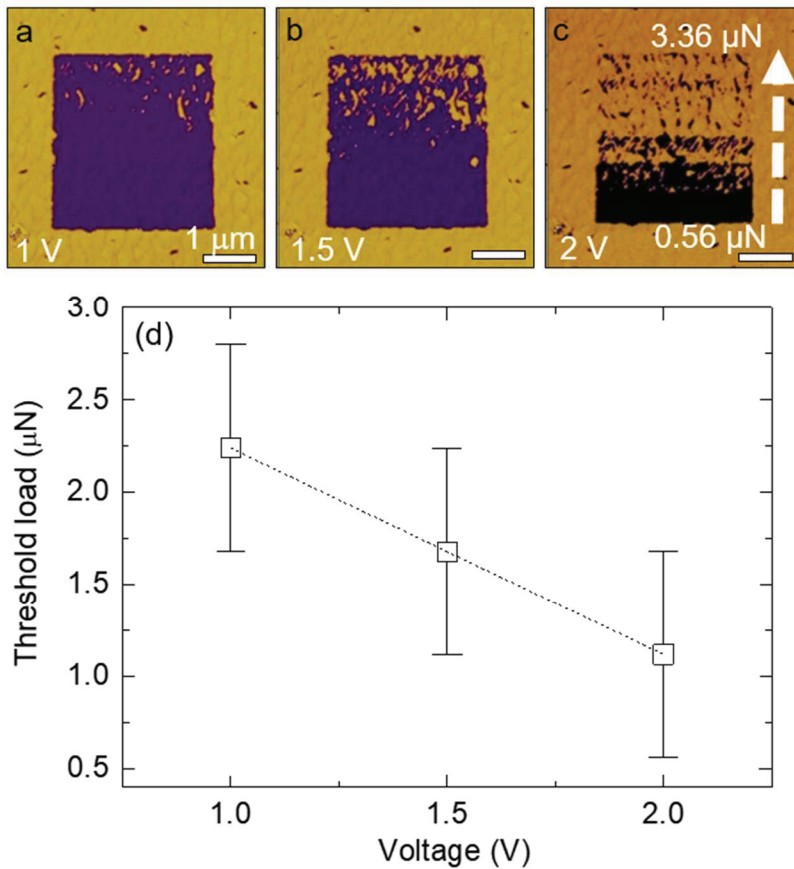
applying electrical bias.

Also, we demonstrated flexoelectric control of electrical state in ultrathin dielectric films. We explained this huge resistivity change in terms of tunable depolarization field by controlling the amount of flexoelectric polarization generated inside of the ultrathin dielectric films. Achieving breakdown using very small electric bias, we could prevent extrinsic effect such as Joule heating and permanent damage on sample even though we applied huge electrostatic field by means of flexoelectricity. This work overcomes a long-standing dilemma: the electrical-state switching in dielectrics requires strong fields, but when applied by strong static fields, dielectrics inevitably suffer from irreversible damage. Utilizing universal flexoelectricity, we could develop a general approach to apply non-destructive, strong electrostatic fields in various insulating systems, such as the Mott insulator. Also, our results can be extended to realize future novel devices such as flexoelectric switch and transistor.

Lastly, there can be many interesting topics we can further study with this AFM tip pressing technique. Since force applied by AFM tip will generate local strain gradients, thus breaking of local inversion symmetry, any change of physical properties or intriguing phenomena induced by the inversion symmetry breaking such as band gap opening in graphene or photovoltaic in centrosymmetric materials can be studied. As those studies would be original in aspect that mechanism is novel flexoelectricity, it would provide good chances for high-impact publications.

Appendix

A. Estimation of conversion factor between electric bias and mechanical force



Scaling OP flexoelectric field a–c, The OP PFM images obtained after mechanical writing with gradual increase of applied force from 0.56 μN to 3.36 μN as indicated by white arrow while fixed electric bias of 1 V (a), 1.5 V (b) and 2 V (c) were applied to the tip respectively. **d**, A plot of the threshold load as a function of the applied tip voltage obtained using data above.

We estimated the flexoelectric field in the mono-domain BFO thin film to switch the polarization by establishing a correlation between the mechanical force and equivalent electric bias. The ferroelectric domain in the BFO film can be switched with voltage less than coercive voltage if the switching process is aided by mechanical force. It is legitimate to think that the verge between two phases corresponds to the region where the sum of the electric bias and the force-induced flexoelectric field in OP component is identical to the coercive voltage. We first upwardly polled the $3 \times 3 \mu\text{m}^2$ region with the application of -7V . After that, while applying a dc voltage to the tip, the upwardly polled area has been scanned with the application of incrementally increasing mechanical force from $0.56\mu\text{N}$ to $3.36\mu\text{N}$ (Fig. a–c). Depending on the applied dc bias, the area of switched domain varied and the correlation between mechanical force and equivalent dc bias was established (Fig. d). According to our analysis, the proportionality coefficient between mechanical force and dc bias is about $1.1 \mu\text{N/V}$ which is consistent in terms of the order recently reported [Očenášek, J. *et al. Phys. Rev. B* **92**, 035417 (2015).].

Finally, we just note that there is another possibility to interpret the above experimental results differently. When the stress is applied on the ferroelectric film, it could move the system towards the high symmetry state, where the polar susceptibility is greater resulting the decreased coercive electric field, thus leading

to the inaccuracy of the conversion factor we obtained. However, this alternative mechanism is not relevant with the directional dependent switching behaviour.

B. Phase field simulation

Phase-field Simulations. The present phase-field model of BFO involves two sets of order parameters, namely, the ferroelectric order parameter, that is, electric polarization (\mathbf{P}), and the antiferrodistortive (AFD) order parameter, that is, the oxygen octahedral rotation ($\boldsymbol{\theta}$) [Xue, F., Gu, Y., Liang, L., Wang, Y. & Chen, L. Q. *Phys. Rev. B* **90**, 220101 (2014)]. The kinetics of both order parameters are described by the time-dependent Landau-Ginzburg (TDGL) equation, namely,

$$\frac{\partial \boldsymbol{\eta}}{\partial t} = -M \frac{\delta \mathbf{F}(\boldsymbol{\eta})}{\delta \boldsymbol{\eta}}$$

where $\boldsymbol{\eta}$ is the order parameter (either \mathbf{P} or $\boldsymbol{\theta}$), M is the kinetic coefficient, and \mathbf{F} is the total free energy. The total free energy for \mathbf{P} and $\boldsymbol{\theta}$ contains bulk energy, elastic energy, electric energy, flexoelectric energy, and domain wall energy. The details of each contribution have been well documented in our previous publications [Xue, F., Gu, Y., Liang, L., Wang, Y. & Chen, L. Q. *Phys. Rev. B* **90**, 220101 (2014)., Li, Y. L., Hu, S. Y., Liu, Z. K. & Chen, L. Q. *Acta Mater.* **50**, 395–411 (2002)., Gu, Y., Hong, Z., Britson, J. & Chen, L.-Q. *Appl. Phys. Lett.* **106**, 022904 (2015).].

The tip-induced stress on the surface is described by Hertz contact theory of a spherical indenter with a ~ 10 nm contact radius at 5 μN . The frictional shear stress $\sigma_{31}(\mathbf{r})$ is assumed to be proportional to the compressive normal stress $\sigma_{33}(\mathbf{r})$ by

$k = 0.3$. The normal and shear stress distributions on the film surface are superimposed with stress-free boundary conditions at the top surface while -1.5% clamped boundary conditions are used at the film-substrate interface. These mixed mechanical boundary conditions and short circuit electrical boundary conditions were adopted, for the elastostatic and electrostatic equilibrium solved at each timestep, respectively. The procedure for solving the fully anisotropic elastostatic and electrostatic equations has been systematically described in our previous work [Li, Y. L., Hu, S. Y., Liu, Z. K. & Chen, L. Q. *Acta Mater.* **50**, 395–411 (2002).]. The three-dimensional system was discretized with 64x64x40 grid points to solve the two coupled TDGL equations by semi-implicit Fourier transformation [Chen, L.-Q. & Shen, J. *Comput. Phys. Commun.* **108**, 147–158 (1998).]. All of the key parameters followed the previous work on BFO [Xue, F., Gu, Y., Liang, L., Wang, Y. & Chen, L. Q. *Phys. Rev. B* **90**, 220101 (2014).], which were fitted from experiments and first-principles calculations. Owing to the lack of flexoelectric coefficients reported for BFO, we adopted a conservative estimation for the flexocoupling constants for pseudocubic BFO as $f_{11} = 5$ V, $f_{12} = 5$ V and $f_{44} = 1$ V, which is within the theoretical values of general perovskites (1-10 V). To simulate the STO substrate with a 4° miscut angle toward the [110] direction, two sets of coordinates, namely, global (x', y', z') and local crystallographic (x, y, z)

coordinates, were adopted, following the routine described in our previous work [Winchester, B., Wu, P. & Chen, L. Q. *Appl. Phys. Lett.* **99**, 052903 (2011).].

Simulation of strain profile. The strain distribution in a 3.9 nm-thick STO thin film pressed with an AFM tip is obtained by solving the elastic equilibrium equation in a 3D thin film/substrate system with appropriate boundary conditions. The detailed procedure is described in previous works [Li, Y. L., Hu, S. Y., Liu, Z. K. & Chen, L. Q. *Acta Mater.* **50**, 395–411 (2002).]. Here, we discretized three-dimensional space into $100 \times 100 \times 500$ grid points and applied periodic boundary conditions along the x_1 and x_2 axes. The grid spacing was $\Delta x_1 = \Delta x_2 = 0.5$ nm and $\Delta x_3 = 0.1$ nm. Along the x_3 direction, 35 layers were used to mimic the film; the relaxation depth of the substrate featured 350 layers to ensure that the displacement was negligibly small. To estimate the surface stress distribution that developed with AFM-tip pressing, we adopted the closed-form solution derived by Wang *et al.* for indentation responses in a piezoelectric thin film in the ultrathin-film limit [Wang, J. H., Chen, C. Q. & Lu, T. J. *J Mech. Phys. Solids* **56**, 3331–3351 (2008).]. This contact mechanics model, comparing to the classical Hertz model for a non-piezoelectric, semi-infinite space, considers not only the finite size of the film but also the coupled nature of the indentation problem of an electromechanically active sample. Therefore, it is more appropriate to describe the surface stress caused by nano-indentation in ultrathin STO films in the present work.

We considered an STO thin film of thickness h_f , with the top surface in contact with an AFM tip and the bottom interface coherently constrained by the substrate. We assumed a conductive, rigid, spherical indenter with a tip radius $R = 150$ nm and a mechanical force F ranging from 1 to 25 μN . At the top surface, the

normal stress distribution (as a function of the distance from the contact center) is described as follows:

$$\sigma_{33}^{tip}(r) = \begin{cases} -c_{33}P \frac{(a^2 - r^2)}{2h_{def}}, & r \leq a \\ 0, & r \geq a \end{cases}$$

where a is the contact radius ($a = \sqrt{2R(h_{ind} + \frac{e_{33}}{c_{33}}\phi_0)}$), h_{ind} is the indentation depth

($h_{ind} = \sqrt{\frac{Fh_{def}}{c_{33}\pi R} - \frac{e_{33}}{c_{33}}\phi_0}$), h_{def} is the deformation depth $h_{def} = h_f$, c_{33} is the elastic

stiffness of the STO film ($c_{33} = 336$ GPa), e_{33} is the piezoelectric coefficient of the STO film ($e_{33} = 0$ C m⁻²), and ϕ_0 is the applied bias ($\phi_0 = 0$ V). At the film–substrate interface, the displacement is continuous for coherency and is assumed to relax to zero within a depth of h_s into the substrate (i.e., $\eta_i|_{x_3=-h_s} = 0$). The clamping effect of the STO substrate is considered to render the average strain zero at each layer of the film (i.e., $\overline{u_{11}} = \overline{u_{22}} = 0$ and $\overline{u_{12}} = 0$). Finally, the boundary value problem of elastic equilibrium, assuming no body force, is given by

$$\begin{cases} \sigma_{ij,j} = 0 \\ \sigma_{33}|_{x_3=h_f} = \sigma_{33}^{tip}, \sigma_{31}|_{x_3=h_f} = \sigma_{32}|_{x_3=h_f} = 0 \\ \eta_i|_{x_3=-h_s} = 0 \end{cases}$$

where stress is related to strain via $\sigma_{ij} = c_{ijkl}e_{kl} = c_{ijkl}(u_{kl} - u_{kl}^0)$. The eigenstrain u_{ij}^0

is derived from strain-order parameter couplings of STO through $u_{ij}^0 = Q_{ijkl}P_kP_l + \lambda_{ijkl}q_kq_l$, where Q_{ijkl} and λ_{ijkl} are the electrostrictive and rotostrictive tensors, respectively. The electrostrictive and rotostrictive coupling coefficients of STO were adapted from ref. [Li, Y. L. *et al. Phys. Rev. B* **73**, 184112 (2006).].

Simulation of the polarization profile. The polarization distribution under the mechanical load by an AFM tip can be calculated by self-consistent phase-field modeling. The temporal evolution of the polarization field $\mathbf{P}(\mathbf{x},t)$ is governed by the time-dependent Ginzburg–Landau equation, i.e., $\partial\mathbf{P}/\partial t = -L(\delta F(\mathbf{P})/\delta\mathbf{P})$, where L is the kinetic coefficient and the total free energy F can be expressed as

$$\begin{aligned}
F &= \int (f_{\text{bulk}} + f_{\text{elastic}} + f_{\text{electric}} + f_{\text{gradient}} + f_{\text{flexo}}) dV \\
&= \int [\alpha_{ij}P_iP_j + \alpha_{ijkl}P_iP_jP_kP_l + \beta_{ij}\theta_i\theta_j + \beta_{ijkl}\theta_i\theta_j\theta_k\theta_l + t_{ijkl}P_iP_j\theta_k\theta_l + \frac{1}{2}g_{ijkl}\frac{\partial P_i}{\partial x_j}\frac{\partial P_k}{\partial x_l} \\
&\quad + \frac{1}{2}k_{ijkl}\frac{\partial \theta_i}{\partial x_j}\frac{\partial \theta_k}{\partial x_l} + \frac{1}{2}c_{ijkl}(u_{ij} - u_{ij}^0)(u_{kl} - u_{kl}^0) - \frac{1}{2}E_iP_i + \frac{1}{2}f_{ijkl}(\frac{\partial P_k}{\partial x_l}\varepsilon_{ij} - \frac{\partial \varepsilon_{ij}}{\partial x_l}P_k)] dV
\end{aligned}$$

The bulk Landau free energy f_{bulk} consists of two sets of order parameters, i.e., the spontaneous polarization \mathbf{P} and the antiferrodistortive order parameter $\boldsymbol{\theta}$, which represents the oxygen octahedral rotation angle of STO. The flexoelectric contribution is considered as a Lifshitz invariant term as

$$f_{\text{flexo}} = \frac{1}{2}f_{ijkl}(\frac{\partial P_k}{\partial x_l}u_{ij} - \frac{\partial u_{ij}}{\partial x_l}P_k)$$

The eigenstrain tensor \mathbf{u}^0 in the elastic energy density is given by

$$u_{ij}^0 = Q_{ijkl}P_kP_l + \Lambda_{ijkl}\theta_k\theta_l - F_{ijkl}P_{k,l}$$

in which the electrostrictive, rotostrictive, and converse flexoelectric couplings are considered via tensors \mathbf{Q} , $\mathbf{\Lambda}$ and \mathbf{F} . The coefficients used in constructing the total free energy F of an STO single crystal are given in our previous works [Li, Y. L. *et al.* Phase transitions and domain structures in strained pseudocubic (100) SrTiO₃ thin films. *Phys. Rev. B* **73**, 184112 (2006)., Sheng, G. *et al.* *J. Appl. Phys.* **108**, 084113 (2010).]. The transverse flexoelectric constant of STO estimated from experiments in the present work was used ($f_{12} = 25$ V); the other two flexoelectric components were assumed to be zero (i.e., $f_{11} = f_{44} = 0$) for simplicity.

C. First-principles calculations

First-principles calculations. The atomic and electronic structures of the system were obtained using density functional theory (DFT) implemented in the Vienna ab initio simulation package (VASP). The projected augmented plane wave (PAW) method was used to approximate the electron-ion potential. The exchange and correlation potentials were calculated using the local spin density approximation (LSDA). In the calculations, we employed a kinetic energy cutoff of 340 eV for PAW expansion, and a $6 \times 6 \times 1$ grid of \mathbf{k} points for Brillouin zone integration. The in-plane lattice constant was that of relaxed bulk STO ($a = 3.86 \text{ \AA}$); the c/a ratio and internal atomic coordinates were relaxed until the Hellman–Feynman force on each atom fell below $|0.01| \text{ eV \AA}^{-1}$.

To understand the effect of electronic polarization on the interfacial electronic structure, we constructed a SrRuO₃/STO bilayer with five unit cells of SrRuO₃ and nine layers of STO, part of which is shown in Fig. 4.2a. The sub-interfacial layers of the completely relaxed paraelectric phase of STO on SrRuO₃ are insulating, and the Fermi level lies in the gap between the conduction band minima and valence band maxima. However, when STO is highly polarized, the induced electrostatic field largely bends bands; thus, both the conduction band minimum and valence band maximum of sub-interfacial STO layers could cross the

Fermi level, as shown in the LDOS plot (Fig. 4.2b). We plotted Fig. 4.2b with frozen uniform displacement of the Ti atom by 0.18 and 0.54 Å. Note that polarized tetragonal STO has higher energy than paraelectric cubic STO, but can be stabilized under non-equilibrium strain conditions. This band profile clearly supports the experimental finding that the band crossing of STO conduction and valence bands could lead to a colossal decrease in the electrical resistivity.

The dielectric constant was calculated using density functional perturbation theory. Fig. 4.6 represents the calculated total zz component of the total dielectric constant (i.e., ϵ_{zz}), which includes both ionic and electronic contributions, as a function of strain u . The strain was measured with respect to the DFT equilibrium lattice of 3.86 Å.

In order to investigate the change in the band gap of STO in the presence of the strain, we have used the hybrid functional (HSE06) implemented in the VASP package (Fig. 4.7). We have used 5-atom unit cell to simulate unstrained cubic and strained tetragonal structures in which an $8 \times 8 \times 8$ \mathbf{k} -point grid with energy cut-off of 600 eV are used. Convergence is reached if the consecutive energy difference is within 0.01 meV for electronic iterations and 0.1 meV for ionic relaxations. The calculated lattice constant of the cubic structure by full structure relaxation is 3.897 Å with a band gap of 3.3 eV, in good agreement with experimental data [van Benthem, K., Elsässer, C. & French, R. H., *J. Appl. Phys.* **90**, 6156–6154 (2001).]. For the strained tetragonal unit cell, a unit cell with compressive strain of 2%, 2%, and 10% for a , b , and c lattice constants with respect to the relaxed cubic structure

is considered based on the strain profile simulation. The calculated band gap of the tetragonal structure is around 3.6 eV, slightly larger than that of the cubic structure.

Wentzel–Kramers–Brillouin simulation. Using the one-dimensional WKB approximation, we can simply describe the tunneling current density for a low T and small V , as follows:

$$\begin{aligned}
 j(V) &= \frac{2e}{h} \int_{-\infty}^{\infty} T(E) \times [f(E) - f(E - eV)] dE \\
 &\cong \frac{2e}{h} \int_{-\infty}^{\infty} \exp\left(-\frac{4\pi}{h} \int_0^d \sqrt{2m(U(x) - E)} dx\right) \times [f(E) - f(E - eV)] dE \\
 &\cong \frac{2e}{h} \exp\left(-\frac{4\pi}{h} \int_0^d \sqrt{2m(U(x) - E_F)} dx\right) \times eV
 \end{aligned}
 \tag{4}$$

where $T(E)$, $f(E)$, $U(x)$, and m represent the transmission probability, Fermi–Dirac distribution, tunnel barrier profile, and free electron mass, respectively. Using equation (4), we obtain the tunneling current density for a trapezoidal barrier profile (Fig. 4.3) as follows:

$$\begin{aligned}
 j(+V) &= \frac{2e}{h} \exp\left(-\frac{4\pi}{h} \int_0^{d_0} \sqrt{2m \left\{ \frac{\varphi_2 - \varphi_1 + eV}{d_0} (x - d_0) + \varphi_2 \right\}} dx\right) \times eV \\
 &= \frac{2e}{h} \exp\left(-\frac{8\pi\sqrt{2m}}{3h} \cdot d_0 \cdot \frac{(\varphi_2)^{1.5} - (\varphi_1 - eV)^{1.5}}{\varphi_2 - \varphi_1 + eV}\right) \times eV
 \end{aligned}$$

$$\begin{aligned}
j(-V) &= -\frac{2e}{h} \exp\left(-\frac{4\pi}{h} \int_0^{d_0} \sqrt{2m \left\{ \frac{\phi_2 - \phi_1 - eV}{d_0} (x - d_0) + \phi_2 - eV \right\}} dx\right) \times eV \\
&= -\frac{2e}{h} \exp\left(-\frac{8\pi\sqrt{2m}}{3h} \cdot d_0 \cdot \frac{(\phi_2 - eV)^{1.5} - (\phi_1)^{1.5}}{\phi_2 - \phi_1 - eV}\right) \times eV
\end{aligned}$$

where ϕ_2 and ϕ_1 are the barrier heights of the right and left sides of the trapezoidal barrier, respectively, i.e., $\phi_2 = \phi_0 + \Delta\phi$ and $\phi_1 = \phi_0 - \Delta\phi$. Using equation (4), we can also obtain the tunneling current density for a triangular barrier profile (Fig. 4.3) as follows:

$$\begin{aligned}
j(+V) &= \frac{2e}{h} \exp\left(-\frac{4\pi}{h} \int_0^{d'} \sqrt{2m \left\{ \frac{\phi}{d'} (x - d') + \phi \right\}} dx\right) \times eV \\
&= \frac{2e}{h} \exp\left(-\frac{8\pi\sqrt{2m}}{3h} \cdot d' \cdot \frac{\phi^{1.5}}{\phi + eV}\right) \times eV
\end{aligned}$$

$$\begin{aligned}
j(-V) &= -\frac{2e}{h} \exp\left(-\frac{4\pi}{h} \int_0^d \sqrt{2m \left\{ \frac{\phi - eV}{d} (x - d) + \phi - eV \right\}} dx\right) \times eV \\
&= -\frac{2e}{h} \exp\left(-\frac{8\pi\sqrt{2m}}{3h} \cdot d \cdot (\phi - eV)^{0.5}\right) \times eV
\end{aligned}$$

where ϕ and d indicate the barrier height and width of the triangular barrier, and $d' = d \cdot \phi / (\phi + eV)$. Importantly, depending on whether we consider the contribution of the STO valence band, ϕ and d have a different dependence on $\Delta\phi$. When neglecting the STO valence band, $\phi = \phi_0 + \Delta\phi$ and $d = d_0 \cdot [(\phi_0 + \Delta\phi) / 2\Delta\phi]$ (Fig. 4.3a); this

indicates that although the increased $\Delta\phi$ reduces the barrier width d , it also increases the barrier height ϕ , such that the overall tunneling conductance cannot become largely enhanced (as shown in Fig 4.11b; black dashed line). In striking contrast, when considering the STO valence band, ϕ is fixed to Δ_{bg} and $d = d_0 \cdot \Delta_{\text{bg}} / 2\Delta\phi$ (Fig. 4.3b), which could lead to colossal enhancement of the tunneling conductance with increasing $\Delta\phi$ (Fig. 4.1b).

D. Detailed sample characterization

Sample fabrication. SrRuO₃ and STO thin films were sequentially grown on TiO₂-terminated and (100)-oriented STO substrates. The growth dynamics and thickness were monitored by in-situ reflection high-energy electron diffraction (RHEED; Fig. 4.8). Film deposition was performed at 700°C under oxygen partial pressure of 100 and 7 mTorr for SrRuO₃ and STO, respectively. After deposition, films were annealed at 475°C for 1 h in oxygen at ambient pressure and subsequently cooled to room temperature at 50°C min⁻¹. Structural characterization, namely, reciprocal space mapping was performed to ensure that the STO film was strain-free.

Tunneling measurements. The I - V curves were obtained using an Asylum Research Cypher AFM (Oxford Instruments, Abingdon, UK) at room temperature under ambient conditions. Conducting diamond-coated metallic tips (DDESP-V2; BRUKER, Billerica, MA, USA) with nominal spring constants 80 N m⁻¹ and a dual-gain ORCA module (Oxford Instruments) were used to measure currents. An electrical bias was applied through the conducting SrRuO₃ electrode; this was swiped from -0.5 V to +0.5 V at a ramping rate of about 4 V s⁻¹. During the measurements, we set the current limit (compliance) to 20 nA. The noise floor of the AFM system was about ~few pA. We measured the resistance R from the linear slope of I - V curves in the low-bias regime. We extracted the resistance of STO, i.e., R_{STO} , from the difference between the measured R and the resistance of the bottom

SrRuO₃ layer (i.e., ~70.4 kΩ; Fig. 4.10i). We then estimated an effective resistivity (ρ_{eff}) of STO by considering the effective tip-STO contact radius (a) and the effective STO thickness (t_{STO}):

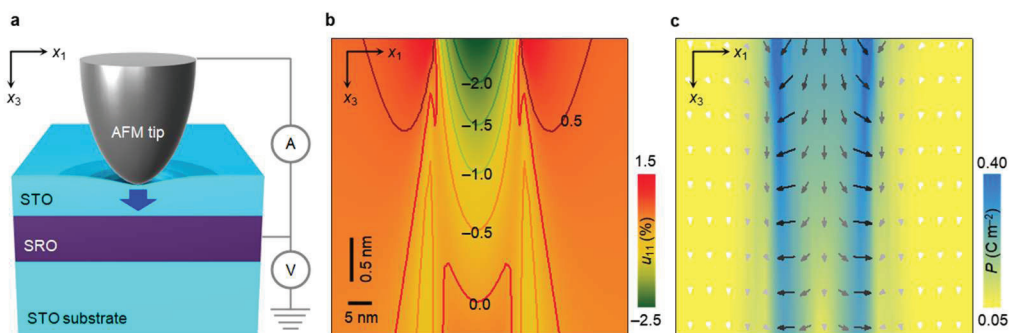
$$\rho_{\text{eff}} = R_{\text{STO}} \cdot \frac{\pi a^2}{t_{\text{STO}}}$$

where we obtained the values of a and t_{STO} from our theoretical contact mechanics analysis.

Graphene. For the graphene transfer onto the ultrathin BaTiO₃ film, the so-called dry-transfer technique was used. A graphene monolayer was mechanically exfoliated on a silicon wafer coated with poly(vinyl alcohol) (PVA), which is water-soluble, and poly(methyl methacrylate) (PMMA). After the selection of a proper graphene flake, the flake/ PMMA layer was detached from the silicon substrate by immersion in hot deionized water. After that, the flake/PMMA layer floating on the water was transferred to a holder and was placed on the ultrathin BaTiO₃ film using a homemade micromanipulator after alignment under an optical microscope. At last, the PMMA was removed with acetone.

E. Enhanced flexoelectricity at reduced dimensions revealed by mechanically tunable quantum tunneling

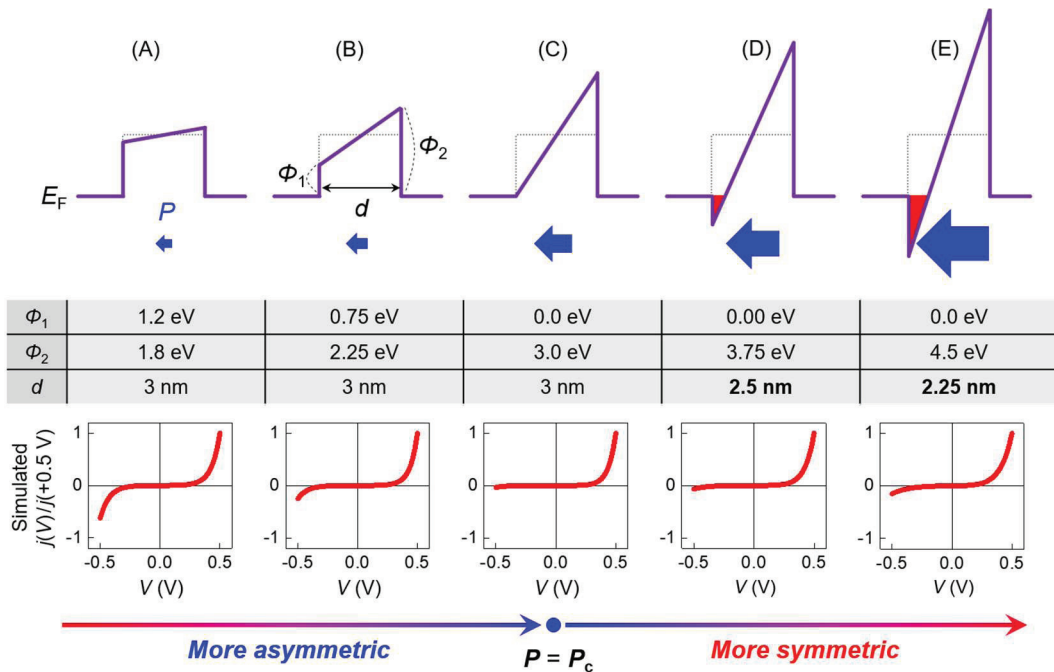
It is also possible to obtain nanoscale flexoelectric coefficient by the experimental method used in Chapter 4. We have published another paper using the method to calculate nanoscale flexoelectric coefficient. Here, short summary of the work is provided. For more details, please see the ref. [S. Das, S. M. Park *et al.*, *Nat. Commun.* **10**, 1–7 (2019).]. Starting from ultrathin 9 u.c. SrTiO₃ film as shown in figure below, we have pressed the film with incremental force by sharp AFM tip.



Mechanically induced large polarization in ultrathin SrTiO₃. (a), Schematic diagram of the experimental setup, illustrating the flexoelectric polarization (blue arrow) generated by the atomic force microscope (AFM) tip pressing the surface of ultrathin SrTiO₃. While generating large strain gradients, we simultaneously measure the tunneling currents across the flexoelectrically polarized STO. (b and c), Phase-field simulations for the transverse strain u_{11} (b) and corresponding polarization distribution (c) in ultrathin SrTiO₃ under a representative tip loading force of 5 μ N over a circular area \sim 13 nm in radius.

As the loading force increases, bend bending occurs as described in Fig. 4.1. While the band bending goes stiffer before the conduction band minimum cross the Fermi level, I-V curve would become asymmetric as the band diagram become more asymmetric as can be seen in Figure below. However, once the conduction band

minimum cross the Fermi level, I-V curve would become more symmetric as the band width decreases. By using this critical point, which conduction band crossing the Fermi level, we can estimate the flexoelectric coefficient exploiting the equation 4.3.



Band diagram and corresponding I-V characteristic while the flexoelectric polarization increases. At the beginning, I-V curve become more asymmetric as the flexoelectric polarization increases. However, it become more symmetric above the point of which the conduction band minimum cross the Fermi level.

Publication List

1. **S. M. Park**, B. Wang, S. Das, S. C. Chae, J. S. Chung, J. G. Yoon, L.-Q. Chen, S. M. Yang, T. W. Noh, “Selective control of multiple ferroelectric switching pathways using a trailing flexoelectric field” *Nature Nanotechnology* **13**, 366-370 (2018)
2. S. Das, B. Wang, T. R. Paudel, **S. M. Park**, E. Y. Tsymbal, L.-Q. Chen, D. Lee, T. W. Noh, “Enhanced flexoelectricity at reduced dimensions revealed by mechanically tunable quantum tunneling.” *Nature Communications* **10**, 537 (2019).
3. **S. M. Park**, B. Wang, T. Paudel, S. Park, J. R. Kim, S. Das, E. K. Ko, H. G. Lee, N. H. Park, D. Suh, E. Y. Tsymbal, L.-Q. Chen, T. W. Noh, D. Lee, “Colossal flexoresistance in dielectrics.” Submitted to *Nature*.
4. H. G. Lee, L. Wang, L. Si, X. He, D. Porter, J. R. Kim, E. K. Ko, **S. M. Park**, B. Kim, A. T. S. Wee, A. Bombardi, Z. Zhong, T. W. Noh, “Surface metal-insulator transition in SrRuO₃ ultra-thin films triggered by surface termination conversion.” Submitted to *Nature Materials*.

국문초록

대칭의 개념은 물리학에서 놀라운 역할을 가지고 있다. 물질이 가지고 있는 대칭의 종류에 따라서 물질이 가질 수 있는 물리적 질서나 특성이 결정된다. 결정 대칭성에 따라서 고체는 잘 알려진 결정질 점군으로 분류될 수 있는데, 1830년에 32가지 유형의 형태학적 결정군으로 분류될 수 있다는 것이 증명되었다. 어떤 결정군에 속해있는지를 통해 복굴절과 같은 광학적 특성이나 압전성과 같은 전기기계적 결합이 나타날 수 있는지 여부를 알 수 있다.

전기적 특성과 기계적 특성 사이의 상관성은 매우 흥미로운 물리적 현상이며, 미시적인 크기의 전자기계부터 압전 액츄에이터, 모터, 센서, 에너지 발전기, 전동기 단백질 및 세포막과 같은 생물 시스템에 이르기까지 다양한 분야에서 사용되고 있다. 전기 기계적 상관성의 가장 보편적인 예는 균일한 변형이 가해질 때 전기장이 물질 내부에 생성되는 압전성이다. 반면에, 불균일한 변형이 물질에 가해지는 경우에도 물질 내부에 전기장이 형성되게 되는데 이를 변전효과라고 한다.

변전효과는 전기적 분극과 불균일한 변형 사이의 상관관계로 정의될 수 있다. 이 현상의 중요성으로서 변전효과가 압전효과보다 더 보편적으로 나타난다. 즉, 더 많은 결정에서 나타날 수 있는 효과이다. 압전성은 32개중에 20개의 결정군에서 나타날 수 있는 반면, 변전성은 32개 모두의 결정군에서 나타날 수 있는 현상이다. 또한 변전효과는 물질의 크기가 작아지면

작아질수록 효과의 크기가 커진다는 재미있는 특성을 가지고 있다. 이러한 특성 때문에 압전효과가 사용되는 장치를 대체할 수 있는 효과로서 매우 큰 물리적 산업적 중요성을 가지고 있다.

본 박사논문에서는 변전효과에 의해 유도되는 반전 대칭 깨트림을 이용하여 산화물 박막의 물리적 특성을 제어하는 것이 가능하다는 것을 보여줄 것이다. 특히, 국소적인 영역에 날카로운 원자힘 현미경의 탐침을 이용하여 압력을 가하는 기술을 사용함으로써 원하는 영역에만 국소적으로 물리적 특성의 변화를 야기해낸 일들을 소개할 것이다. 나의 연구들은 산화물 박막에서 순수한 힘만을 가지고 흥미로운 물리적 현상 또는 특성을 제어하고 관찰하는 것이 가능하다는 것을 시사한다.

핵심단어: 변전효과, 분균일 응력, 국소적인 반전대칭 깨트림 강유전성, 켄썩기 산화물 초박막, 유전 분극, 원자힘 현미경 탐침 누르기.

학번 2014-30111

감사의 글

항상 선배들이 졸업하면서 박사학위 논문을 전해주면 가장 먼저 하는 일이 감사의 글을 확인하는 것이었습니다. 어느덧 세월이 흘러 졸업을 앞두고 감사의 글을 직접 작성하게 되니 이제야 졸업하게 되는 것이 실감이 납니다. 글을 작성하며 생각해보니 대학원생으로서 5년 이상의 세월이 흐르는 동안 참 많은 분들께 여러 가르침과 도움을 받았다고 생각이 됩니다. 이제는 더 이상 학생이 아닌 독립적인 연구자로서 홀로 서게 될 생각을 하니 설렘 반 걱정 반의 생각이 듭니다. 이렇게 박사학위를 받는 과정까지 도움을 주신 많은 분들에게 짧은 글을 통해서나마 감사한 마음을 표현하고자 합니다.

가장 먼저 힘들 때 낙담하고 쓰러지지 않게 붙잡아 주신 하나님께 감사 드립니다. 돌아보자면 학위과정 동안에 그렇게 신실하게 믿음생활을 하지 못한 것 같지만 신앙의 끊을 놓지 않고 살아가는 만으로도 항상 큰 힘이 되었고 삶의 목적과 의미를 잃어버리지 않도록 하는 버팀목이 되어주었습니다. 이번에 글을 쓰는 것을 계기로 좀 더 건실한 믿음을 가지고 굳건하게 신앙생활을 하겠다고 다짐해봅니다.

저에게 지금까지 가장 큰 영향을 주신 분이시자 저의 지도교수님이신 노태원 교수님께 감사를 드립니다. 여러 가지 면에서 부족한 저를 끊임없이 다독여주시고 일깨워주시며, 연구적인 부분뿐만 아니라 사회생활, 사람들과의 관계, 여러 가지 경험들에서 얻으신 노하우 등 많은 부분을 가르쳐 주셨습니다. 교수님 덕분에 쉽게 누릴 수 없는 기회를 얻을 수 있었고 정말 너무나도 많은 점에서 배우고 성장할 수 있었다고 생각합니다. 교수님 밑에서 지도 받을 수 있었던 것을 정말 큰 행운이라고 생각합니다. 항상 저희들이 잘되기를 가장 우선순위로 생각해주시고 전폭적으로 지원해주시는 모습을 앞으로 저도 실천할 수 있는 학자가 되도록 하겠습니다. 항상 프로다움과 리더의 자세를 가지고 살아가겠습니다.

학위과정 동안 연구에 큰 도움을 주시고 지도해주신 양상모, 이대수 그리고 채승철 교수님, 세 분 모두 신임교수 시절 정신 없이 바쁘신 중에도 물심양면으로 저의 연구를 지도해주시고 도와주셔서 정말 감사 드립니다. 저의 주 실험장비인 AFM의 전문가이시면서 꼼꼼하면서도 즉각적인 피드백과 현실적인? 조언으로 지속적으로 도와주신 양상모 교수님. 연구실에 들어와서 처음으로 읽었던 저에게는 교과서와 같았던 논문들의 저자이시자 번뜩이는 아이디어와 스마트함으로 연구의 정점을 보여주신 이대수 교수님. 논문을 작성해본 적이 없어서 아무것도 모르고 답답해 하는 저를 가엽게 여기시고 먼저 다가와주셔서 구원의 손길을 건네주신

채승철 교수님. 논문 쓰는 방법부터 그림 그리는 프로그램까지 처음부터 세심하게 하나하나 가르쳐주시고 실험방향 및 논문 내용도 같이 고민해주시고 본인의 일처럼 도와주신 것 정말 감동이었습니다. 세 분의 도움을 받을 수 있었던 것은 정말 큰 행운이었습니다.

토요일까지 희생해주시며 강유전체 미팅에 참석해 주신 김태현 교수님, 손창희 교수님, 양상모 교수님, 이대수 교수님, 윤종걸 교수님, 장서형 교수님 그리고 정진석 교수님께 감사 드립니다. 미팅 때마다 각 분야의 전문가분들께서 함께해주셔서 항상 든든했고, 전해 주신 수많은 조언들과 질문들이 연구적으로나 발표의 질 향상에 있어서 정말 큰 도움이 되었습니다. 또한 영국유학시절부터 타지에서 힘들지 않을까 걱정해주시고 집에 초청해주셔서 식사까지 대접해주시며 항상 챙겨주시고 도와주신 양운기 교수님께도 감사 드립니다. 아무것도 모르던 저에게 양운기 교수님께서 노태원 교수님 연구실을 추천해주신 덕분에 이렇게 좋은 환경에서 연구를 할 수 있게 되었다고 생각합니다. 더불어 저의 박사 논문 심사를 위해 힘써 주신 이규철 교수님, 이진호 교수님, 이탁희 교수님께도 감사의 말씀을 전해 드립니다. 여러 일로 바쁘신 와중에도 학위 발표를 경청해주시고 다양한 시각에서 연구를 평가해주셔서 감사 드립니다.

공동연구를 진행하였던 연구단 외의 많은 분들께도 감사의 인사를 드립니다. 저의 논문들에 있어서 가장 큰 도움을 주었던 Bo Wang과 Long-Qing Chen 교수님께 감사 드립니다. 또한 제일원리계산으로 많은 도움을 주신 Lingling Tao 박사님, 박세영 박사님, Evgeny Tsybal 교수님께도 감사 드립니다. 여러분의 기여 덕분에 항상 이론적으로 든든하게 주장하는 바를 뒷받침 할 수 있었을 뿐만 아니라 이론가의 시각에서 나온 다양한 질문들은 저의 논문들의 질을 확연하게 높이는 데 큰 도움이 되었습니다. 제가 신입생일 때 정말 좋은 BiFeO₃ 타겟들을 제공해 주신 명환이형, 최고의 그래핀 샘플을 제공해주신 박나희씨, 서동석 교수님, 그리고 정말 구하기 힘든 Ca₃Ti₂O₇ 샘플을 제공해 주신 오운석 교수님께도 감사 드립니다. 많은 분들의 도움 덕에 무사히 박사학위를 받게 됐다고 생각합니다.

오랜기간 생활을 함께했던 연구실 선후배 분들께도 감사의 말씀을 드립니다. 먼저, 제 사수 선배님이시자 처음으로 PLD, XRD, AFM 등 여러 연구장비를 알려주신 병철이형에게 감사 드립니다. 졸업을 앞두고 바쁘신 와중에도 신경 써주셔서 정말 감사하게 생각합니다. 연구실에 들어가서 초반에 형의 기대에 부응하여서 좀 더 열심히 하지 못 한 것이 아쉽습니다. 항상 자리에서 묵묵하게 열심히 일을 하고 계시던 다운이형, 연구실에 들어간지 얼마 안되어서 병철이형과 함께 졸업을 하셔서 많이 친해지지 못하여서 아쉽지만 개인적으로 본받고 싶은 냉철함과 성실함의 끝을

보여주셨습니다. 보기만 해도 즐거웠던 향근이형, 한없는 푸근함과 구수한 사투리, 그리고 특유의 유머감이 아직도 생각이 나네요. 지금은 벌써 교수님이 되신 창희형, 뛰어난 리더십과 유머감각으로 형 덕분에 즐거운 연구실 생활을 할 수 있었습니다. 얼마 전에 울산에 세미나를 하기 위해 내려갔을 때 직접 차로 역까지 마중 나와주시고 밥도 사주시고 정말 감동이었습니다. 묵묵하게 맡은 일 잘하시는 현주누나 수빈이형, 삼성에서도 잘하고 계실 것이라 믿습니다. 항상 듣직했던 영재형 모르는 것을 물어볼 때마다 친절하게 알려주시고 같이 공부하자고 말씀해 주셨던 것이 기억납니다. 예일에서 좋은 연구 많이 하고 돌아오셔서 좋은 직장 잡으시길 바랍니다. 항상 솔선수범 해주시는 인호형, 무슨 일이 생기면 항상 해결책을 구하러 형을 찾게 되는 것 같습니다. 항상 도움만 받은 것 같아서 죄송한 마음이 듭니다. 마음이 따뜻하신 재석이형, 첫 논문을 쓰신 것을 계기로 앞으로도 좋은 연구 많이 할 수 있길 바라겠습니다. ARPES 팀의 브레인 지섭이형, 이제 곧 포닥을 가시게 될 텐데 앞으로 어딜 가시든 잘 해내실 것이라 생각되고 또 바라겠습니다. 요즘 행복해 보이는 우진이형, 졸업과 결혼준비를 병행하시다니 정말 대단합니다. 이제 곧 미국으로 떠나실텐데 앞으로 형의 아재개그가 많이 그리워질 것 같은 강력한 느낌이 드네요. 미국 가서도 행복하시길 바라겠습니다. 단점을 찾아보기 힘든 민철이형, 포닥을 가신지 얼마 되지 않았지만 얼마전에 연구실에서 세미나 하시는 모습을 보면서 벌써 교수님들 못지 않은 포스를 느낄 수 있었습니다. 좋은 결과들 많이 얻고 돌아오시길 바랍니다. 연구실을 먼저 떠나버린 기덕이형과 호동이, 어딜 가든 좋은 일만 가득하기를 바라겠습니다. 연구실의 유일한 동갑친구 소연이, 다른 팀이어서 같이 연구를 하진 않았지만 책임감도 많고 똑똑한 능력자라는 것을 느낄 수 있었습니다. 배울 점이 정말 많은 친구라고 생각합니다. 이번에 같이 졸업을 하지만 연구실을 먼저 나가게 될텐데 가는 곳에서 대성하길 바랍니다.

우리 팀 똑똑한 정래, 후배지만 항상 도움도 많이 받고 여러 면에서 오히려 배우는 것 같습니다. 항상 열심히 하는 모습 대견스럽고 앞으로는 도움을 많이 줄 수 있는 선배가 되도록 노력하겠습니다. 일도 잘하고 즐길 줄도 아는 한결이, 낮은 년차에 방장을 맡게 되어 고생이 많습니다. 항상 고마운 마음을 가지고 있습니다. 이제 곧 훈련소를 가게 될 텐데 몸조심하고 무사히 돌아오기를 바랍니다. 언제나 흥이 넘치는 진권이, 덕분에 가속기 실험을 경험하였습니다. 연구적으로 고민이 많은 것 같은데 지금도 충분히 잘하고 있다고 생각합니다. 앞으로도 꾸준히 열심히 하면 분명 좋은 결과를 얻을 것이라 생각합니다. 같은 팀 착한 막내 지환이, 부탁하지도 않았는데 책상이 더러우면 와서 치워주던 모습이 생각납니다. 후배가 들어오면 잘 챙겨주겠다고 다짐했었는데 그렇지 못한 것 같아 미안합니다. 항상 약을 많이 먹는데 늘 건강하고 행복하길 바랍니다. 늘 밝고 당찬 은교, 항상 열심히 하는 모습이 대견합니다. 콜라보레이터로서도 측정 부탁할 때 마다 군소리 하나 없이 실험을 잘

해 주어서 너무 고맙습니다. 다재다능한 범주, 무주 워크숍에서 발표하는 것을 보았을 때 무엇을 하든 잘할 것이라 생각합니다. 좀 더 교류를 많이 하지 못한 것이 아쉬움이 남습니다. 든든하고 항상 적극적인 정근이, 외국에서 오랫동안 공부하다 와서도 잘 적응 하는 모습 대견합니다. 짧은 시간 안에 좋은 결과를 내야될텐데, 주변 사람들에게 적극적으로 도움도 많이 구하고 열심히 한다면 충분히 잘 할 수 있을 거라 생각합니다. 응원하겠습니다. 연구실에 처음 왔을 때 여러가지 면에서 많은 도움을 주었던 마이클, 샤샤, 첸타이, 다니엘, 같은팀의 링페이, 사이캣, 웨이 박사에게도 감사의 말을 전합니다.

연구단의 다른 직원분들께도 감사드립니다. 지원팀의 박원구 박사님, 이인호 선생님, 강태동 박사님, 김금채 선생님, 배현이 선생님, 김태승 선생님, 조혜인 선생님, 이나현 선생님, 권오성 선생님, 장성진 박사님, 송인경 박사님, 장비 유지 보수 및 수리 등 연구단의 크고 작은 업무에 항상 관여하셔서 아낌없는 도움 주셔서 마음 편히 연구에 집중할 수 있었습니다, 그리고 행정팀의 전지현 실장님, 김정란 선생님, 나고운 성생님, 김서경 선생님, 주양희 선생님, 박주영 선생님, 지정은 선생님, 한나 선생님께 감사드립니다. 직전에 급하게 일처리 하는데도 항상 군말 없이 도와주시고 워크샵 및 연구단 행사에 있어서 항상 큰 도움을 주셨습니다. 정말 감사드립니다.

마지막으로 언제나 저를 믿고 지켜봐 주셨던 부모님께 감사의 마음을 전해드립니다. 무뚝뚝하고 감정 표현에 서툴렀던 아들의 모습에 때론 속상하실 때도 많았겠지만, 내색하지 않고 언제나 저를 응원해 주시고 격려해주셔서 감사 드립니다. 저의 형에게도 감사의 마음을 전합니다. 타지에서 오랫동안 공부하면서 많은 힘든 점들이 있었을 텐데 묵묵히 잘 해내주어서 고맙습니다. 가족들의 사랑 덕분에 지금의 제가 있었다고 생각합니다. 언제나 감사하고 사랑합니다.

많은 분들께 도움을 받았습니다. 여기에 모두 적지는 못하였지만, 앞으로 항상 보답하는 마음으로 언제나 겸손한 마음으로 인생을 살아나가도록 하겠습니다. 다시 한번 감사 드리고 항상 행복하시고 건강하세요.

2019년 7월 28일
박성민